

## CHAPTER 15

# Coupled Mechanical Shear and Hydraulic Flow Behavior of Natural Rock Joints

Mikko P. Ahola<sup>a</sup>, Sitakanta Mohanty<sup>a</sup>, and Axel Makurat<sup>b</sup>

<sup>a</sup>Center for Nuclear Waste Regulatory Analyses, San Antonio, Texas, 78238

<sup>b</sup>Norwegian Geotechnical Institute, P.O. Box 3930, Ullevaal Hageby, N-0806, Oslo, Norway

### 15.1 INTRODUCTION

The coupled mechanical-hydraulic (MH) behavior of rock joints is an important issue in many applications, including the analysis of oil and gas reservoirs as well as deep geologic disposal of nuclear waste. In the case of underground disposal of nuclear waste, accurate prediction of the fluid flux within the near-field waste emplacement area is necessary for assessment of waste package corrosion rates as well as calculations on radionuclide migration to the accessible environment. The host rock environment for siting a repository for nuclear waste has predominantly focused on competent hard rock formations such as granite (e.g., Canadian and Finnish Programs) or welded volcanic tuff (e.g., U.S. Program). Such rock units predominantly have low porosities and matrix permeabilities, such that the majority of the fluid flow through the waste emplacement horizon is likely to be along the natural and induced fractures. Fractures may be induced by excavation of the tunnels, thermal expansion due to heating, seismic motion, and overall long-term deterioration of the near-field rock surrounding the tunnel.

To better understand the coupled MH behavior of natural rock joints as well as to establish a basis for comparison with numerical codes, two experiments have been conducted under DECOVALEX. The focus of this chapter is to provide a comprehensive review of the experimental results, as well as the theories and numerical analyses used by various computer codes to simulate the actual joint response. The first test case experiment (TC1) was conducted by the Norwegian Geotechnical Institute (NGI) using their coupled shear-flow test apparatus. With this apparatus, joints can be closed and sheared under stress controlled conditions while fluid is injected into the fracture. Numerical simulation of this TC1 experiment was also conducted using several computer models with different constitutive relations for the joint. The second test case experiment (TC5) was conducted at the Center for Nuclear Waste Regulatory Analyses (CNWRA) using a direct-shear apparatus modified to include fluid flow within the joint. In this apparatus the fluid is injected along one edge (inlet) of the rectangular joint and simultaneously collected from the opposite edge (outlet), while the remaining two joint edges are sealed to prevent leakage. Thus, it is expected that linear flow takes place between these two inlet and outlet edges. Linear flow experiments were conducted under normal load as well as under combined normal and shear loading on a rock specimen comprised of two blocks of rock bounding a naturally fractured, welded tuff joint.

### 15.2 BACKGROUND

Changes in stress conditions in the near-field rock mass surrounding the emplacement tunnels/boreholes due to excavation, thermal expansion, and possibly seismic loadings result in

incremental deformation along the joints and fractures both in the normal and shear directions (Kana et al., 1991; Hsiung et al., 1992a,b). Laboratory studies on single rock joints have shown that mechanical deformation can have a significant influence on the hydraulic properties of rock joints (Makurat et al., 1990a; Tsang and Witherspoon, 1981). The MH behavior of a deformable rock fracture under pure normal stress has been investigated by Tsang and Witherspoon (1981) and Cook (1992) among others, and appears to be fairly well understood. In most cases under laminar flow conditions in the fracture, the cubic law which relates the flow to the cube of the aperture can be applied with fairly reasonable accuracy. However, for a joint with a high degree of roughness or very small aperture, modification of the cubic law may become necessary (Tsang and Witherspoon, 1981), perhaps because localized flow within the joint is no longer in the laminar regime. Both the mechanical and hydraulic response of rock joints are fairly repeatable after the first several cycles of normal loading, namely behaving in a nonlinear elastic manner with little hysteresis between loading and unloading of the joint. Also, in most cases, normal loading of the joint creates little gouge material due to crushing of asperities as compared to more destructive shear loading, all of which make for easier understanding of the coupled MH behavior of rock joints under normal loading.

It is well known that during joint shear deformation, dilatancy and asperity degradation can modify the flow characteristics (Makurat et al., 1990a; Mohanty et al., 1994). In most cases shear deformation has a much greater impact on the hydraulic properties of joints than normal deformation. There has been an increasing effort to develop a better fundamental understanding of the role of shearing of a fracture on its effective hydraulic aperture (or conductivity). However, the asperity degradation due to shearing and the resulting changes in hydraulic aperture seem to be much more difficult to predict and model than those primarily due to normal joint displacements. The formation of gouge may in some cases restrict the flow, thus reducing the hydraulic conductivity even though the joint is undergoing dilation. The amount of asperity degradation and subsequent gouge production is dependent of the mechanical properties of the rock joint as well as the applied loading state.

Experimental studies have been conducted over the past several years to investigate permeability changes during shear deformation of rock joints. Teufel (1987) conducted shear-flow coupling tests on pre-fractured samples of Coconino sandstone using a triaxial experimental apparatus and showed that the hydraulic conductivity across (i.e., perpendicular to) a fracture decreases with increasing shear deformation because of localized deformation along the fractures and the evolution of a gouge zone. These studies showed that the reduction in permeability across the fracture during sliding on these artificially fractured specimens increased markedly with an increase in effective confining pressure and normal stress across the fracture. Teufel found that for a test conducted at 60 MPa confining pressure and with a normal stress across the fracture of 118 MPa to 132 MPa, the permeability decreased nearly 3 orders of magnitude after a shear displacement of 7.1 mm. This was attributed to the development of a gouge zone between the fractured surfaces, and the progressive decrease in grain size and porosity of the gouge during shear and increasing normal stress. Teufel also observed the creation of microfractures adjacent and subparallel to the sliding surface, the density of which also increased with normal stress. Based on this observation, he suggested that, in sharp contrast to a gouge zone which decreases permeability perpendicular to the fracture, localized microfracturing may create a narrow channel of high

permeability parallel to the fracture. These results, however, may not be directly applicable to similar studies for nuclear waste disposal due to the different rock types involved.

Makurat et al. (1990a) conducted coupled shear deformation and conductivity tests on natural joints for a number of rock types using a biaxial cell. In contrast to Teufel (1987), they measured the hydraulic conductivity along the joint, and concluded that whether the joint conductivity increases or decreases with ongoing shear is dependent on both the joint and rock properties, as well as the stresses applied. The main parameters of importance were suggested to be the uniaxial compressive strength, joint compressive strength, joint roughness coefficient (JRC), normal stress, and shear displacement. It was found that relatively small shear deformations are sufficient to dilate hard rocks and cause joint hydraulic conductivity increases up to two orders of magnitude. They determined that this type of behavior occurred when there was a high ratio of joint compressive strength to applied normal stress ratio as well as a distinct joint roughness morphology. However, it was found that strong mineralization and repeated shearing tended to reduce joint conductivities even in high strength rocks. For soft rocks, it was found that even though dilation occurred during shearing on all joints, not all experienced a resulting increase in hydraulic conductivity. Only those joints with a high value of JRC experienced an increase in permeability. Makurat et al. (1990a) determined decreases in hydraulic conductivity during shearing to be a result of gouge production, which tended to block flow paths and disturb the parallel plate analogy. This is apparently the main reason why existing models developed to predict the coupled flow response during shearing have not agreed well with experimental measurements, as depicted in Figure 15.1, since most do not account for cumulative damage along the joint surface during shear. As shown in Figure 15.1, even if the numerical model takes into account the reduction in asperity height during shear by reducing the joint roughness coefficient, the joint hydraulic conductivity is still overestimated due to the inability to take into account the influence of the gouge.

Experiments were conducted by Esaki et al. (1991) to investigate the shear-dilation-flow characteristics of artificially fractured granite joints extended over displacements well past those corresponding to the peak shear stress. Their goal was to expand the experimental database developed from previous studies to include larger shear displacements and higher normal loads, which would more adequately represent the conditions of actual fractures. In this study, rectangular joint specimens (4.72 cm long by 3.94 cm wide) were tested under normal stresses ranging from 0.2 to 20 MPa with a maximum shear displacement of 20 mm. Results of the coupled shear deformation-flow experiments show that the hydraulic conductivities through the fracture increase by about 1 order of magnitude for the first 5 mm of shear displacement (Figure 15.2a). In the case of high normal stress (i.e., 20 MPa), some joint surfaces were broken by shearing without riding over each other and the hydraulic conductivity increased significantly. During reverse shearing, the hydraulic conductivity was found to be slightly lower than that during forward shearing, essentially following the same response as the dilation. It was found that the hydraulic conductivity was somewhat higher at the initial shearing position after one complete shear cycle was completed for all normal loads. It should be noted that, in these experiments, the flow was radially injected from a hole in the bottom block, and the joint area was not conserved during shearing, the latter of which may be partially responsible for the reported changes in hydraulic conductivity.

Esaki et al. (1992) conducted further studies which concluded that the shear-dilation-flow characteristics of artificially fractured granite are very different from those of sandstone because

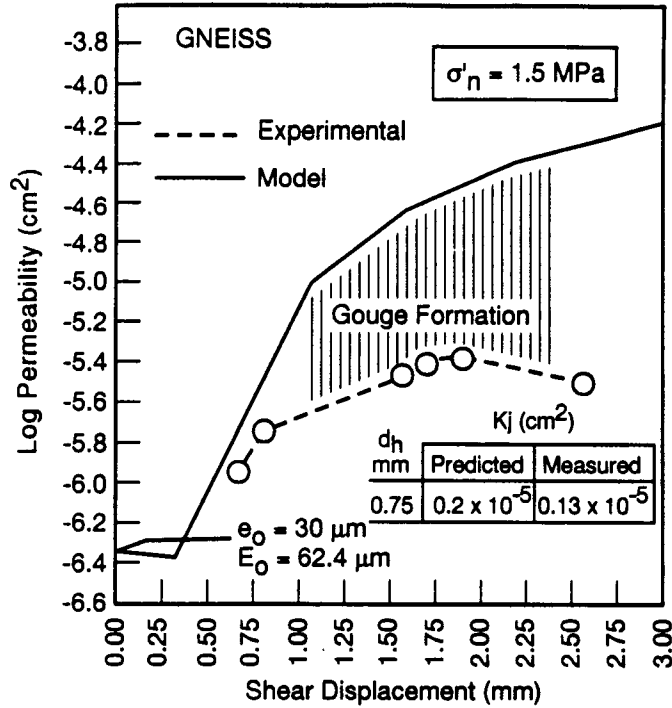
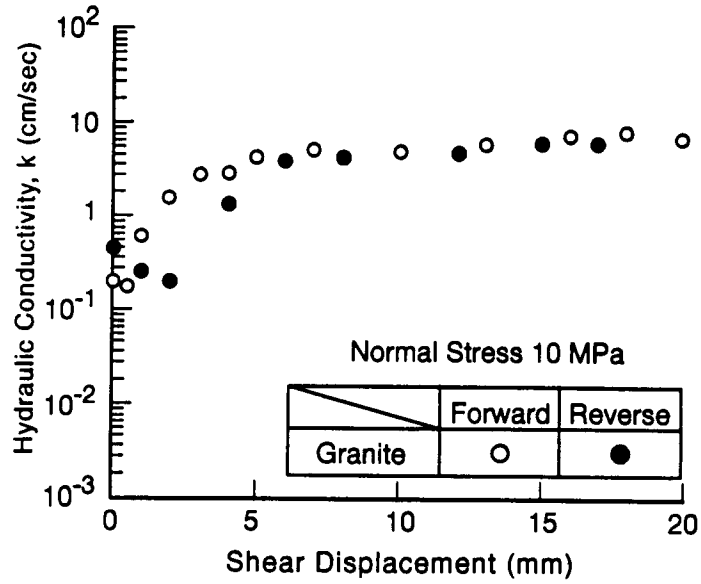


Figure 15.1. Comparison between predicted and measured joint conductivity during joint shearing (after Makurat et al., 1990a).

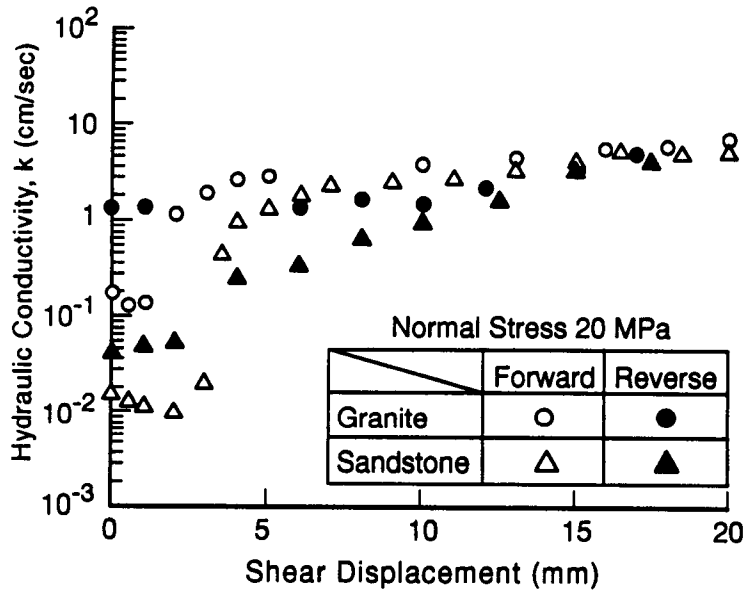
of the difference in the uniaxial compressive strength of the two rock types (162 MPa for granite and 37 MPa for sandstone). In the case of sandstone, the hydraulic conductivity increased rapidly and over a much broader range than in a similar test on granite (Figure 15.2b). This is in spite of the fact that the dilation in the sandstone was much more restrained and consequently lower than that in the granite due to its higher ratio of normal stress to joint compressive strength. In addition, because of the larger amount of gouge created by shear deformation in the case of sandstone, the decrease of hydraulic conductivity during reverse shearing is more dramatic, as shown in Figure 15.2b.

Boulon et al. (1993) also studied the influence of rock joint degradation during shearing on the hydraulic conductivity of granitic rock joints. They proposed a model describing the flow changes which is locally based on the cubic law and taking into account the asperity degradation. They determined that their model generally exhibited a smaller deviation from experimental measurements than the cubic law.

Many investigators (Jing et al., 1994; Makurat et al., 1990b) conducted MH numerical modeling studies on fractures. Most, if not all, numerical models of rock joints do not account for the production of gouge within the joints and its effect on the subsequent flow or pressure drop along the joint. Consequently, it is not surprising that the numerical predictions of the hydromechanical response of rock joints under shear have not tended to agree well with experimental measurements (Jing et al., 1994).



(a)



(b)

Figure 15.2. Hydraulic conductivity-shear displacement diagram for (a) artificially fractured granite under 10 MPa normal load, and (b) sandstone and granite under 20 MPa normal load (after Esaki et al., 1991;1992).

### 15.3 MECHANICAL-HYDROLOGICAL STUDIES ON NATURAL ROCK JOINTS UNDER DECOVALEX

The first TC was formulated by NGI making use of their Coupled Shear Flow Temperature (CSFT) test apparatus. Two individual experiments were conducted under this TC. The first, referred to as Test Case 1, Phase 1 (TC1:1), consisted of both normal and shear deformation coupled with fluid flow through a natural rock joint with fairly low roughness ( $JRC=1.9$ ) as determined using the standard approach proposed by Barton and Choubey (1977). For TC1:1, a very simplified representation of the experimental apparatus was supplied to the modeling teams. For the second experiment, referred to as Test Case 1, Phase 2 (TC1:2), a natural joint with much higher roughness ( $JRC=6.3$ ) was tested to provide higher peak shear response of the joint under coupled mechanical-hydrological shear deformation. Based on lessons learned in the modeling of TC1:1, it was recommended for this second experiment that a much more detailed representation of the experimental apparatus be provided for the modeling of TC1:2.

The second TC, referred to as TC5, was formulated by the CNWRA making use of their direct shear testing apparatus modified to include fluid flow through a joint. The experiment similarly was intended to study the hydro-mechanical response of natural rock joints under combined normal and shear loading. The experimental apparatus and type of rock tested were much different from those of TC1, and the magnitude of shear displacement was significantly higher. Sections 15.2.1 and 15.2.2 discuss in detail each of these two test cases.

#### 15.3.1 Coupled Shear-Flow Test (DECOVALEX Test Case 1)

To better understand the relationship between joint displacement and joint conductivity, a CSFT testing facility was designed and built by NGI (Makurat, 1985). TC1 was conducted using this apparatus, which involved a single rock joint. The test involved several normal stress cycles followed by shear cycling; it involved modeling of specific stress and fluid pressure boundary conditions, and materials (steel, epoxy cement, rock) with different mechanical properties and interfaces. The two experiments conducted by NGI within DECOVALEX serve as calibration exercises for the different joint behavior models used in the codes (continuum and discontinuum) of the DECOVALEX participants.

##### 15.3.1.1 Experimental Apparatus

The CSFT testing equipment is able to close and shear (maximum 5 mm) rough joints under controlled normal stress conditions while simultaneously injecting fluid into the joint. The CSFT test is designed to simulate as closely as possible the *in situ* (stressed, "closed") state of single joints and their alteration by increasing or decreasing normal and shear stresses. Normal-load induced closure and shear-induced dilation of the joint can be caused by these stress changes.

A horizontal cross section through NGI's CSFT apparatus for testing single joints is shown in Figure 15.3. The maximum normal stress acting across the joint depends on the joint surface area, which for the sample in TC1:2 was approximately  $135 \text{ cm}^2$ . However, the maximum allowable flatjack pressure is 25 MPa operating on an area of approximately  $300 \text{ cm}^2$ . Each part of the sample is cast into a reinforced concrete block, such that the joint is oriented 45 degrees with respect to the sides of the concrete block and the principle stress direction. The two blocks containing the sample are mounted into the apparatus with flatjacks acting on each of four sides as shown in Figure 15.3. Flatjack pressures are controlled by two hydraulic pumps.

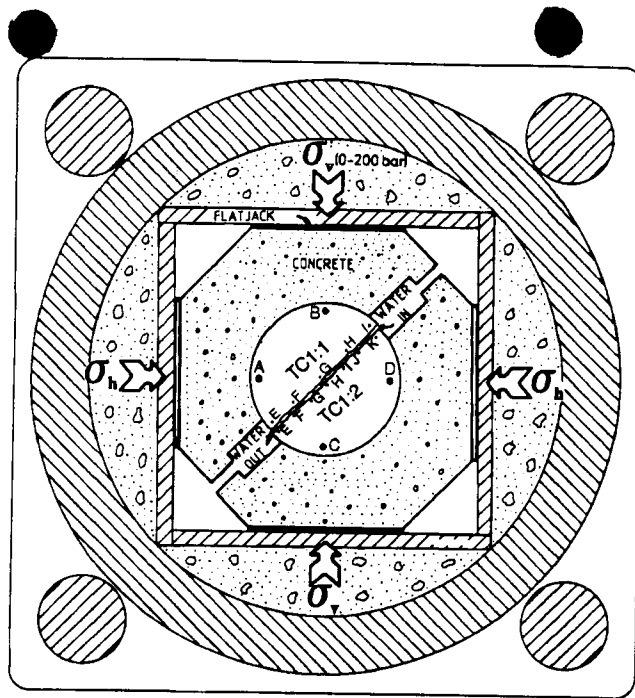


Figure 15.3. NGI's biaxial cell for coupled shear flow testing (CSFT) of natural rough joints.

Displacements normal to the joint (normal displacement) and displacements along the joint (shear displacement) are measured during all stages of the test by four normal displacement and two shear displacement Linear Variable Differential Transformers (LVDT's). LVDT mounting points are referred to as points A, B, C, and D as illustrated in Figure 15.3.

The effective hydraulic aperture of the joint is calculated from the fluid flow rate that passes through the joint (in the horizontal direction) under a constant fluid pressure according to the following relation (e.g., cubic law)

$$e = \left[ \frac{12Qv}{gwi} \right]^{1/3} \quad (15-1)$$

where

- e - effective hydraulic joint aperture (m)
- Q - flow rate (m<sup>3</sup>/s)
- v - kinematic viscosity (m<sup>2</sup>/s)
- g - gravitational acceleration (m/s<sup>2</sup>)
- w - width of flow path (m)
- i - hydraulic gradient between joint ends (-)

The joint is subjected to three normal stress cycles with the maximum normal stress being equal to the smaller of 60% of the joint compressive strength (JCS) and that obtained at the maximum flatjack inflation pressures. For the TC1:2 experiment, the maximum normal stress applied to the rock joint was 25 MPa. During the fourth cycle, the joint is loaded to the normal stress level under which the shear part of the test was conducted. As long as the same oil pressure is applied to

the four flatjacks, only normal stress acts across the joint. This is followed by a shearing stage conducted under constant normal stress. Shear displacement along the joint is created by reducing the oil pressure in two opposite flatjacks by the same increment as it is increased in the other two, so that the normal stress acting on the joint remains approximately constant.

**15.3.1.2 Numerical Simulation of Joint Behavior under Shearing**

The two CSFT tests simulated during the DECOVALEX are referred to as TC1:1 and TC1:2. Both test cases consist of a sequence A (normal loading stage) and a sequence B (combined normal and shear loading stage). However, only sequence B is discussed in this chapter. A discussion of the normal loading results (i.e., sequence A) for TC1:1 and TC1:2 as well as their numerical simulations are given by Makurat et al. (1995) and Jing et al. (1993, 1994). TC1:1 and TC1:2 were modeled by four and three research teams, respectively (see Table 15.1). In the case of the two experiments, pore pressures as predicted by various research teams were small compared to the boundary stresses applied. Several teams thus chose to simulate the tests as uncoupled processes and switch on fluid flow after every normal load variation or shear increment.

**Table 15.1. The TC1:1 and TC1:2 research teams and computer codes**

Research Team	Code	Hardware	Comments
AECL <sup>1</sup>	MOTIF	VAX Station 3100M38	TC1:2: Only sequence A
CNWRA <sup>2</sup>	UDEC	Sun IPX Sparcstation	TC1:1
ITASCA <sup>3</sup>	UDEC	Gateway 486, 33 MHz	TC1:1
LBL <sup>4</sup>	ROCMAS	IBM Risk 6000	TC1:1 Sequence B incomplete TC1:2
NGI <sup>5</sup>	UDEC	DEC 5000/125 Work- station	TC1:1 TC1:2

<sup>1</sup> Atomic Energy of Canada Limited, Pinawa, Manitoba

<sup>2</sup> Center for Nuclear Waste Regulatory Analyses, San Antonio, Texas

<sup>3</sup> Itasca Consulting Group, Inc., Minneapolis, Minnesota

<sup>4</sup> Lawrence Berkeley Laboratory, Earth Science Division, Berkeley, California

<sup>5</sup> Norwegian Geotechnical Institute, Oslo, Norway

UDEC was used by three teams (Itasca, CNWRA, and NGI). UDEC is a two-dimensional code for coupled thermal-mechanical (TM) analysis of discrete block systems and coupled MH analysis through discontinuities (Cundall and Hart, 1985). The simulated rock mass is assumed to consist of an assemblage of discrete blocks interfaced by discontinuities. The parallel plate anal-

ogy is assumed for fluid flow through the joints, while the matrix is impermeable. All three teams used the Barton-Bandis (BB) joint model (Bandis et al., 1983) for their simulations.

In the BB-model, the two components of joint deformation, namely, normal and shear displacements are both based on the scale dependant index properties JRC and JCS, (Barton et al., 1985). The principal shear strength-displacement behavior is described by the following two generalized equations:

$$\sigma_s = \sigma_n \tan \left[ JRC_{mob} \log \left( \frac{JCS}{\sigma_n} \right) + \phi_r \right] \quad (15-2)$$

$$d_{n(mob)} = \frac{1}{2} JRC_{mob} \log \left( \frac{\sigma_1 - \sigma_3}{\sigma'_n} \right) \quad (15-3)$$

where

- $\sigma_s$  - shear stress (MPa)
- $JRC_{mob}$  - the full-scale mobilized JRC at a given displacement (-)
- JCS - joint compressive strength (MPa)
- $\phi_r$  - residual friction angle (degrees)
- $\sigma_n$  - effective normal stress (MPa)
- $d_{n(mob)}$  - full-scale mobilized dilation angle at any given displacement (degrees)

Lawrence Berkeley Laboratory (LBL) used the code ROCMAS which is a three-dimensional (3D) finite element code for solution of coupled thermal-mechanical-hydrologic (TMH) processes in geological systems (Noorishad et al., 1984). The code considers the stress-strain equation and the law of static equilibrium for both the intact rock elements and the joint elements. The discontinuities are represented explicitly as four-noded joint elements with strain-softening behavior for stress analysis and as one-dimensional line elements for fluid flow in discontinuities. The peak shear stress of the joints is based on the Landanyi and Archambault (1970) criterion. The peak shear strength  $\tau_p$  is given by:

$$\tau_p = \frac{\sigma (1 - a_s) (\dot{v} + \tan \phi_\mu) + a_s S_R}{1 - (1 - a_s) \dot{v} \tan \phi_\mu} \quad (15-4)$$

where

- $a_s$  - proportion of joint area sheared through the asperities (-)
- $\dot{v}$  - dilation rate at peak shear stress (-)
- $\phi_\mu$  - friction angle of the sliding surface (degrees)
- $S_R$  - shear strength of the rock composing the asperities (MPa)

The asperity shear strength  $S_R$  is calculated by Ladanyi's equation as:

$$S_R = q_u \frac{\sqrt{1+n}-1}{n} \left[ 1 + (n\sigma)/q_u \right]^{\frac{1}{2}} \quad (15-5)$$

where

- $q_u$  = unconfined compressive strength (MPa)
- $n$  = ratio of compressive strength to tensile strength of the rock composing the asperities (-)

For  $\sigma < \sigma_T$  Landanyi and Archambault (1970) suggest the following power laws for  $\dot{\nu}$  and  $a_s$ :

$$a_s = 1 - \left( 1 - \frac{\sigma}{\sigma_T} \right)^{K_1} \quad (15-6)$$

$$\dot{\nu} = \left( 1 - \frac{\sigma}{\sigma_T} \right)^{K_2} \tan i_o \quad (15-7)$$

where

- $\sigma_T$  = transition stress at which the joint ceases to be weaker than the rock (MPa)
- $K_1$  = 1.5 (-)
- $K_2$  = 4.0 (-)
- $i_o$  = effective roughness at  $\sigma = 0$  (degrees)

The parallel plate model is used for the joint permeability calculations.

Atomic Energy of Canada, Ltd. (AECL) used the 3D finite element code MOTIF, which solves for the coupled fluid flow, heat- and solute-transport processes, and the mechanical deformation of the rock (Guvanasen and Chan, 1990). The solid matrix is assumed to be linearly poroelastic, transversely isotropic, and thermoelastic. The fractures are modeled using the BB joint model and both conduction and convection are considered for heat transport. The solid matrix is represented by 8-noded hexahedral elements. Fractures are represented by 4-noded quadrilateral elements for the flow and heat analysis, and by 8-noded quadrilateral joint elements for stress analysis.

### 15.3.1.3 Material Properties and Boundary Conditions

For TC1:1 the modeling teams were supplied with a simplified geometry of the experiment, whereas for TC1:2 a detailed description of the biaxial experiment was provided. Table 15.2 summarizes the rock and joint material properties of TC2:1 and TC1:2 as specified to the modeling teams. Table 15.3 gives the loading sequences for TC1:1 and TC1:2 as specified to the modeling teams.

**Table 15.2. Material properties for TC1:1 and TC1:2**

property		steel	epoxy & epoxy-rock interface	rock & rock joint	fluid	unit
E Young's modulus	TC1:1	200000	10000	55000		MPa
	TC1:2	200000	25000	55000		
$\nu$ Poisson's ratio		0.27	0.30	0.25		
$\rho$ density	TC1:1	7.00	2.25	2.60	1.00	10 <sup>3</sup> kg/m <sup>3</sup>
	TC1:2	7.00	2.40	2.60		
JCS <sub>j</sub> joint wall compressive strength	TC1:1			150		MPa
	TC1:2			87.1		
JRC <sub>j</sub> joint surface roughness	TC1:1			1.9		
	TC1:2			6.3		
L <sub>j</sub> sample joint length	TC1:1			0.19		m
	TC1:2			0.09		
$\phi_r$ residual friction angle	TC1:1			26.5		degree
	TC1:2			28.7		
dynamic fluid viscosity					0.001	Ns/m <sup>2</sup>

**Table 15.3. Loading sequence for TC1:1 and TC1:2**

Sequence	TC1:1	TC1:2
A	one normal loading cycle (4th cycle in CSFT experiment)	nominal joint normal stress 0→25→0 MPa
B	4 mm forward shear, followed by 4 mm reverse shear	one normal loading cycle (3rd cycle in CSFT experiment) nominal joint normal stress 0→26→0 MPa
		2.8 mm shear nominal joint normal stress 16.5 MPa

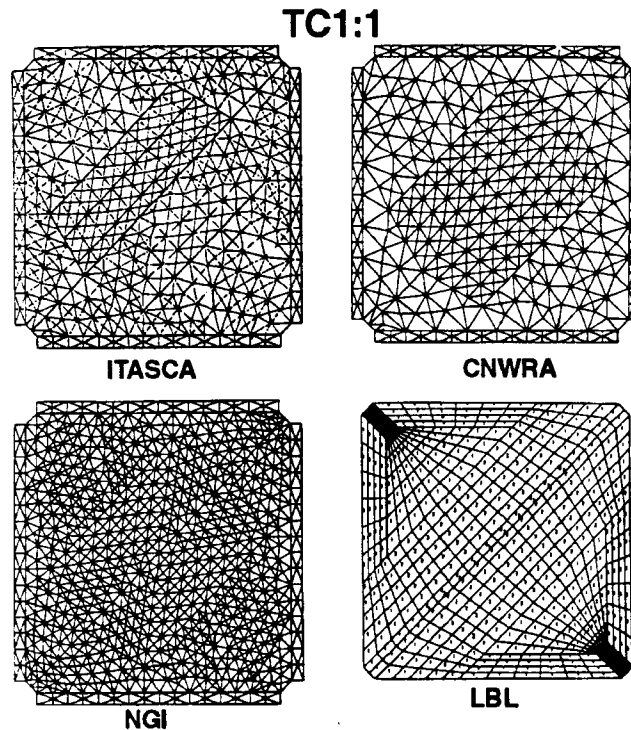


Figure 15.4. Discretization of the TC1:1 model geometry.

#### 15.3.14 Experimental and Numerical Simulation Results for TC1:1

Results are presented for selected shear displacement values for sequence B (i.e., combined normal and shearing portion of the experiment). The monitoring points A to D correspond to the LVDT positions in the CSFT setup, whereas points E to I (TC1:1) and E to K (TC1:2) are fictitious output monitoring points in the joint plane which were used to compare results from different codes (Figure 15.3). Results referring to points A to D are not corrected for intact rock deformation.

Figure 15.4 illustrates the discretizations of the model adopted by the different teams. Itasca, CNWRA, and NGI included the steel plates into their model, whereas LBL modeled only the epoxy block. All teams used stress boundary conditions during the normal joint loading prior to shear, however, the modeling teams used different approaches and assumptions to simulate the shear stage of TC1:1. Itasca and the CNWRA used displacement boundaries and assumed a dilation angle of 0.5 degrees in order to maintain the constant normal stress condition. NGI used stress boundary conditions, accepting that though the equilibrium condition might not be satisfied after the peak shear stress is reached (after 1.68 mm of shear displacement), UDEC tries to satisfy the tabulated  $U_s - \sigma_s$  relationship in the BB-model and thus gives the correct joint apertures.

The LBL team did not include the steel plates in their model geometry. This resulted in large stress concentrations which prevented shear failure. Hence only the three UDEC simulations by CNWRA, Itasca, and NGI are compared. Due to the same modeling approach of CNWRA and Itasca with respect to the boundary conditions and an assumed constant dilation angle of 0.5 degrees over the total joint length, their shear stress-shear displacement curves are quite similar (Figure 15.5). Compared to these, the NGI shear stresses are 5 to 10 MPa higher. This can be

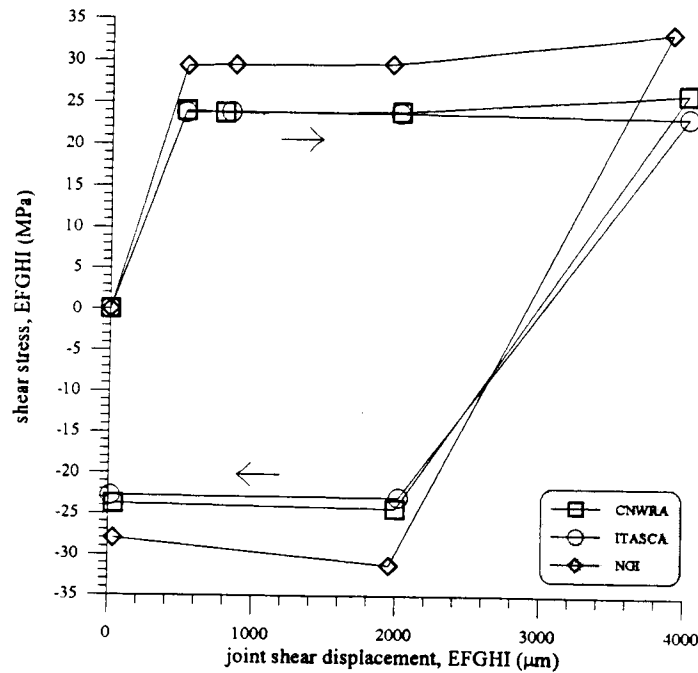


Figure 15.5. Forward and reverse shear stress shear displacement curve for TC1:1.

explained by the stress boundary-induced higher joint end normal stresses. Due to the low JRC, none of the teams predicted substantial joint dilation ( $< 1 \mu\text{m}$ ), measured at points E to I. This is in contrast to the experimental results, which indicate about  $90 \mu\text{m}$  dilation over the first  $1000\text{-}\mu\text{m}$  of shear displacement (Figure 15.6). Both Itasca and CNWRA predict an  $8\text{-}10 \mu\text{m}$  increase in hydraulic aperture from the initial value during forward shear (Figure 15.7). The experimental results also show a maximum change in hydraulic aperture of around  $8 \mu\text{m}$  during shear. The NGI calculated hydraulic apertures lie close to the upper part of the experimental range. The results of the other teams are higher by  $10\text{-}20 \mu\text{m}$ . No experimental data exist for the reverse shear part of the cycle. All teams predicted a substantial increase of hydraulic aperture during reverse shear, which is in contrast to experimental data demonstrating the joint conductivity decreased due to continuous joint surface degradation and associated gouge production during shear cycling (Makurat, 1990a; Mohanty et al., 1994).

#### 15.3.1.5 Experimental and Numerical Simulation Results for TC1:2

The combination of low joint surface roughness ( $JRC_0=1.9$ ) and high normal stresses during shear resulted in non-peak dominated stress strain curves and little dilation in TC1:1. A joint with higher roughness was therefore chosen for TC1:2 (see Table 15.2). The sample comes from the Borrowdale Volcanic Group and challenges the teams to model dilation and strain softening behavior after the peak shear stress.

TC1:2 was modeled by AECL, LBL, and NGI, however, AECL simulated only the normal loading sequence of TC1:2 (sequence A). Again, only the results for the shearing portion of the experiment are presented herein. Figure 15.3 shows the location of the measurement points A to D (now inside the epoxy block), and E to K along the joint plane. In order to avoid over-representa-

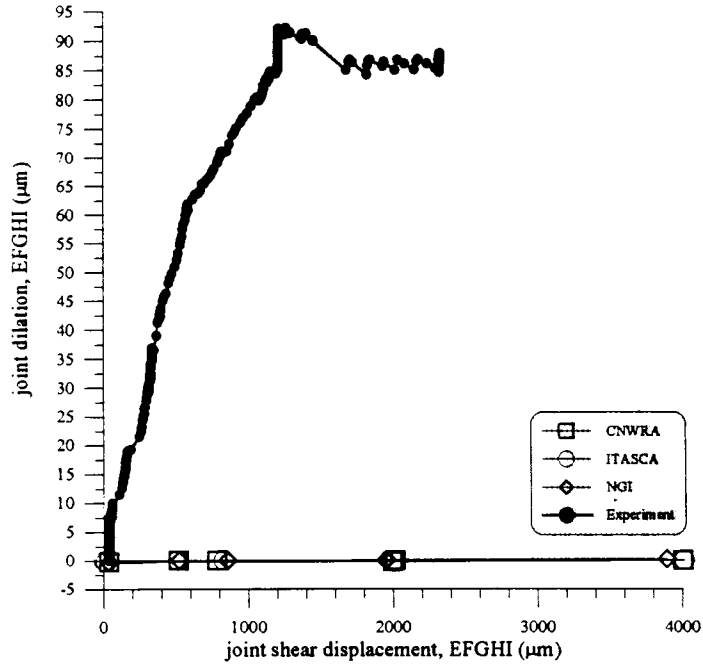


Figure 15.6. Comparison between experimental data and the simulated average joint dilation at points E-I.

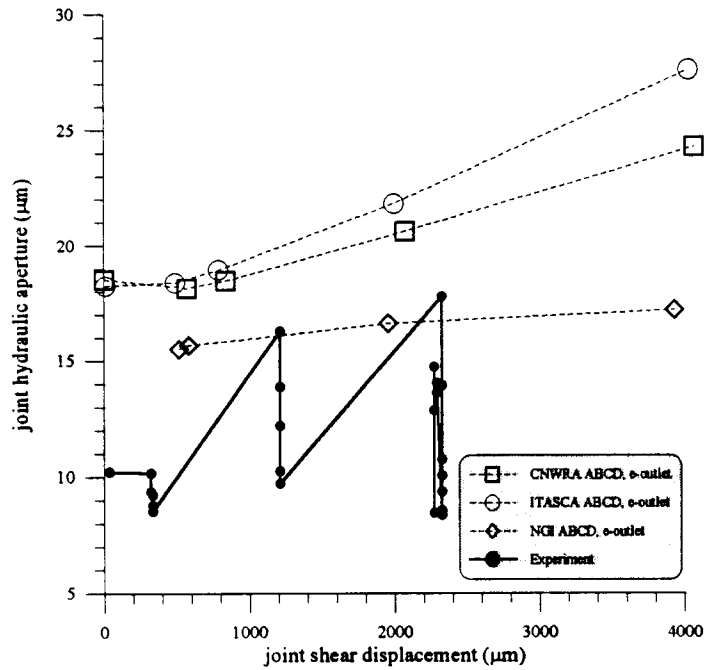


Figure 15.7. Comparison between experimental data and the simulated variation of the joint hydraulic aperture at outlet vs. shear displacement between points A-D.

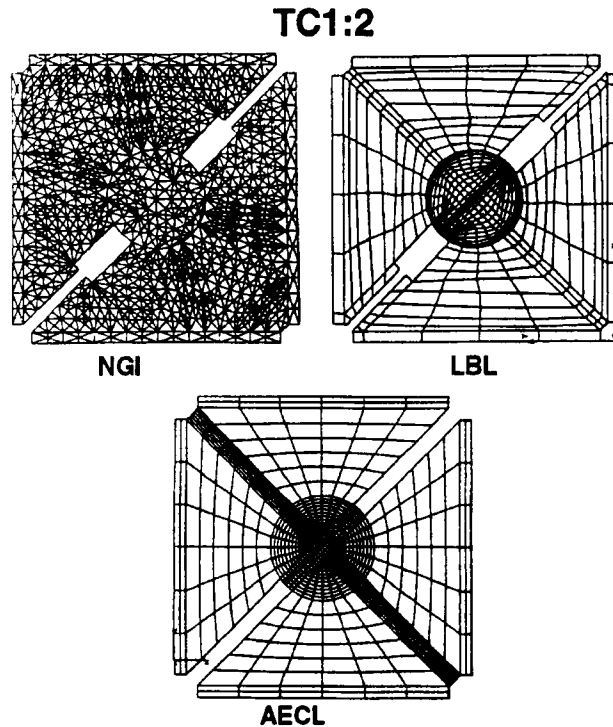


Figure 15.8. Discretization of the TC1:2 model geometry.

tion of the over-stressed joint edge points, average values along the joint plane included only points F to J.

All teams included the steel plates into their models. LBL used four-node finite elements with linear displacement interpolation for the intact material, and four-node joint elements with linear interpolation of the displacements and fluid pressure fields. NGI split the model into two separate blocks with the joint as the interface (Figure 15.8). The shearing sequence was modeled by LBL using a “stabilized boundary load driven” system. The system consists of a combination of stress boundaries and a small high shear stiffness element in the joint plane. In the pre-failure range, every joint element acts as an individual spring, and the stabilizer, which deforms much less, will have no bearing on the response of the other joint elements. After failure of an element, all released load of the failed element is absorbed by the stiff linear stabilizer element. NGI modeled sequence B by applying a mixed boundary system, similar to a direct shear box loading principle. This is achieved by combining the direct application of the required normal stress to the outer boundary of one block with a velocity boundary condition on the other block. In order to avoid block tilting, the system is completed by zero displacement boundaries perpendicular to the applied normal stress and perpendicular to the applied velocity boundary.

As stated earlier, sequence B was modeled only by LBL and NGI for TC1:2. The experimental results indicate 500  $\mu\text{m}$  mechanical dilation under 2800  $\mu\text{m}$  shear displacement (Figure 15.9). The BB model predicts about 80  $\mu\text{m}$  dilation at 2800  $\mu\text{m}$  shear displacement, and 10.8 MPa peak shear strength at 730  $\mu\text{m}$  peak shear displacement. Consequently, the constitutive models in UDEC and ROCMAS are not capable of modeling this obviously non-BB joint behavior. The LBL simulation (65  $\mu\text{m}$  dilation) is rather close to the 1D-predicted 80  $\mu\text{m}$  dilation obtained by NGI. NGI’s results are strongly affected by tilting of the upper block, resulting in 30  $\mu\text{m}$  dilation

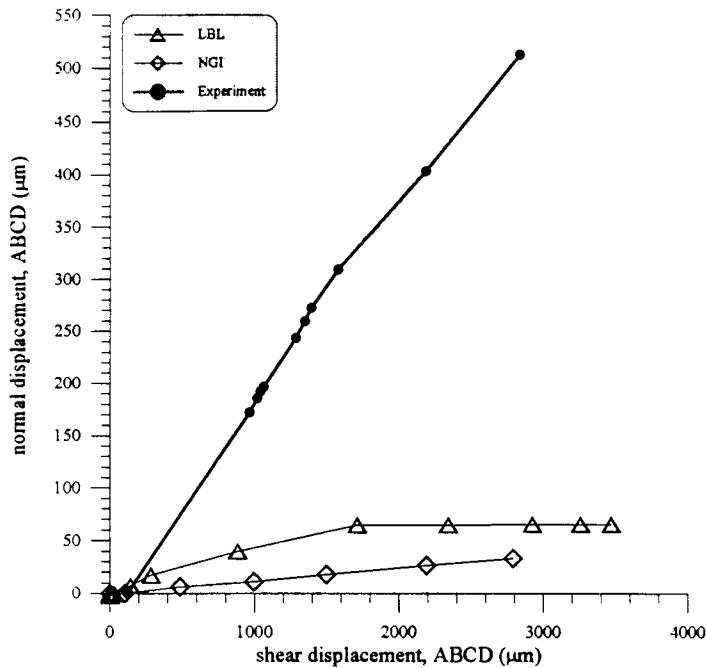


Figure 15.9. Comparison between experimental data and the simulated joint dilation between points A-D.

at one joint end and 100  $\mu\text{m}$  closure at the other end. Experimental results also indicate a dramatic increase in hydraulic joint aperture from 52 to 222  $\mu\text{m}$  during 0 to 100  $\mu\text{m}$  shear, and a residual hydraulic aperture of 72  $\mu\text{m}$  after 2100  $\mu\text{m}$  shear (Figure 15.10). The NGI results are again influenced by the tilting of the top block, and show a continuous increase in joint aperture with shear. The LBL simulation seems to settle at a residual aperture similar to the experimental residual aperture. The stress strain curves are given in Figure 15.11. Since the LBL model did not experience any type of block rotation during shear, the results for the joint elements match perfectly the one-dimensional simulated BB stress strain curve. NGI overpredicts the peak shear stress by about 2 MPa and peak shear displacement by about 600  $\mu\text{m}$ .

### 15.3.2 Direct Shear-Flow Test (DECOVALEX Test Case 5)

As a part of Phase III of DECOVALEX, a Test Case was also proposed by the CNWRA to investigate the coupled MH fluid flow behavior through a natural rough fracture as a result of both normal and shear deformation along the fracture. The experiment was conducted using the CNWRA direct shear testing apparatus (Hsiung et al., 1993) which was modified to allow linear fluid flow experiments to be conducted within the joint under combined normal and shear loads (Mohanty et al., 1994). Linear fluid flow experiments were conducted under normal stresses up to 8.0 MPa, as well as shear displacements up to 2.54 cm under constant normal stresses of 2.0, 4.0, and 5.0 MPa.

#### 15.3.2.1 General Description of Apparatus and Experimental Setup

To conduct coupled MH experiments on single jointed rock specimens, the CNWRA basic servocontrolled direct shear test apparatus with combined normal and shear loading capability

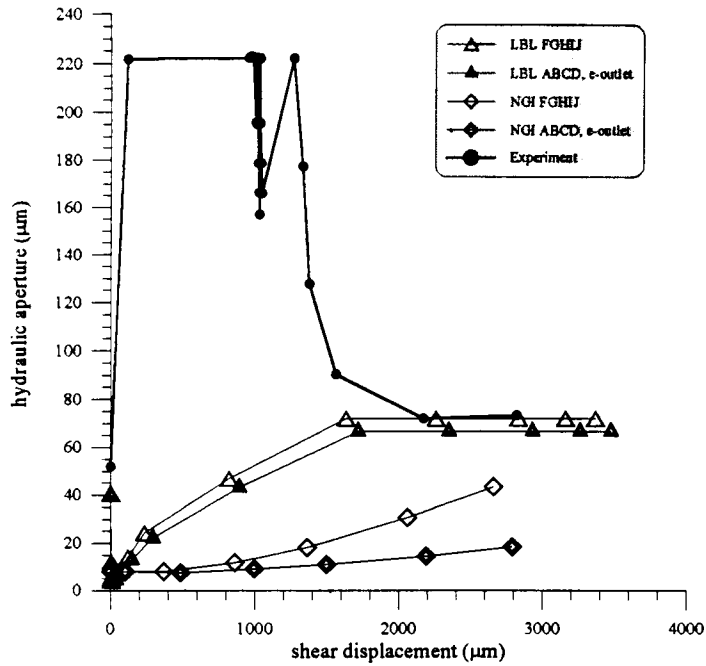


Figure 15.10. Comparison between experimental data and the simulated variation of the joint hydraulic aperture at outlet vs. shear displacement between points A-D and F-J.

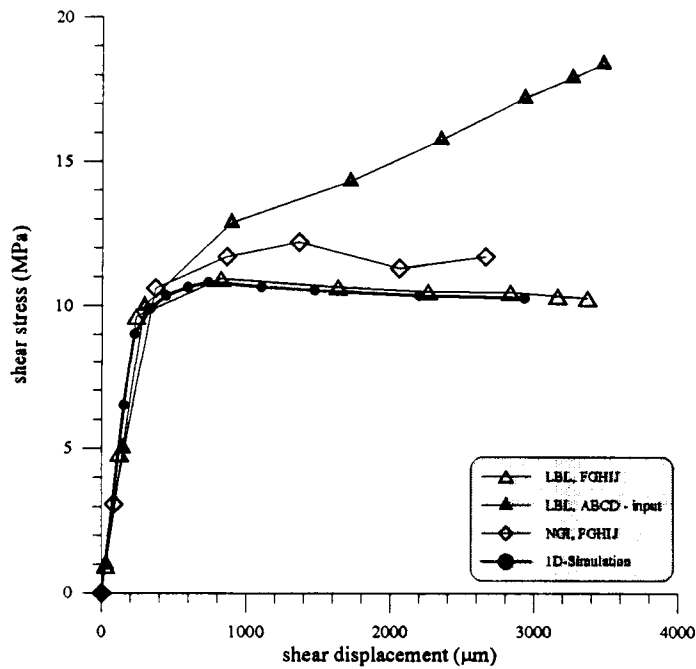


Figure 15.11. Comparison between the 2D simulated stress strain behavior and the 1D joint stress strain curve.

was modified to include the necessary hydrologic system. A brief description of this basic apparatus is given in the following sections. A more detailed discussion is given by Kana et al. (1990) and Hsiung et al. (1993). Figure 15.12 shows the overall mechanical loading apparatus and associated data channels. The modification made to the basic apparatus to include the necessary hydraulic system is discussed in Section 15.3.2.4, although a more in-depth discussion is given by Mohanty et al., (1994).

The apparatus consists of vertical and horizontal servocontrolled loading actuators, reaction frames, shear box fixtures, and an instrumented jointed tuff specimen. The loading capacity for each of the three vertical actuators is 0.133 MN, and 0.222 MN is the loading capacity for the horizontal actuator. For the MH experiments, the horizontal actuator is operated in a displacement control mode, with the displacement ramped pseudostatically. Each vertical actuator is equipped with a 0.111-MN capacity load cell for monitoring the applied forces. The instrumentation for monitoring the applied normal load is arranged to provide an analog output for the sum of the three load cells, as well as for the individual signals. The bottom shear box was designed to house a specimen with maximum dimensions of 0.305×0.203×0.102 m. The top shear box houses a specimen with maximum dimensions of 0.203×0.203×0.102 m. Both are grouted in their respective specimen boxes. The bottom shear box and other fixed devices are bolted to a 1.22×2.13×0.15 m thick steel base plate for rigidity. The horizontal translation of the top shear box along the direction of shearing is guided through three rollers between the top shear box and normal load frame. It is also guided through side rollers. Thus, the normal load frame and the side rollers prevent rotation of the vertical actuators (and therefore also the top specimen block) about a vertical axis perpendicular to the direction of shearing.

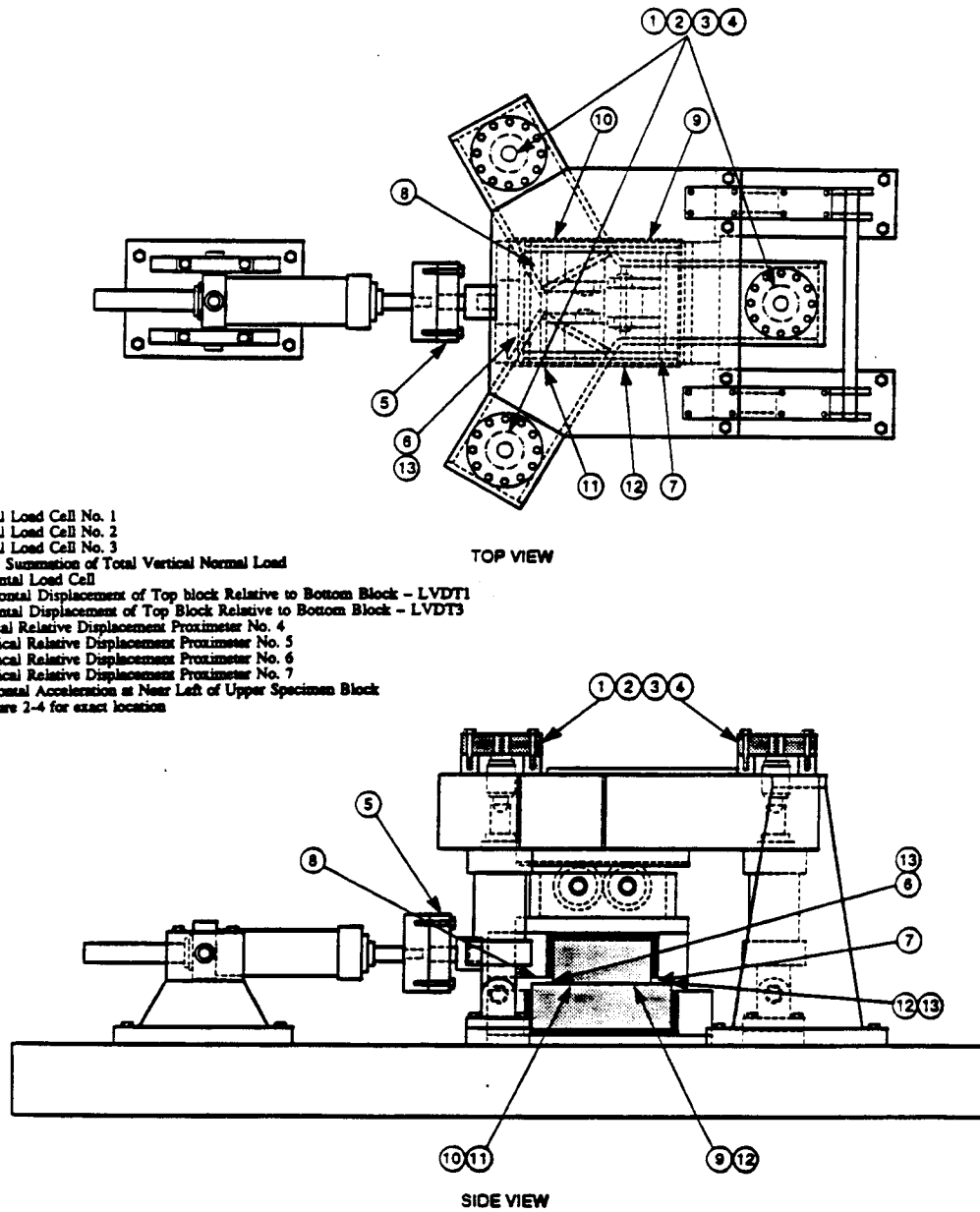
#### **15.3.2.2 Normal Mechanical Load System**

Normal compression is applied to the specimen by three vertical actuators set at 120° about the specimen's vertical centerline. These actuators act through individual load cells whose output is summed and used as the control signal. Thus, the total normal load is controlled at a pre-selected static or slowly ramped value. This total resultant load is ultimately applied to the specimen via the normal load frame which acts on the three normal load rollers (see top view of Figure 15.12) and thereby on the upper specimen box. The line of action for this normal load is through the null position of the upper specimen box. Thus the normal load frame is constrained to three degrees of freedom:

- (i) Vertical translation
- (ii) Rotation about the horizontal axis in line with the shear
- (iii) Rotation about the horizontal axis transverse to the shear

These constraints are assured by two double flexures which connect the normal load frame to a fixed reaction brace, and by the two side roller assemblies, which act on the upper specimen box. Thus, the upper specimen block is constrained to these same degrees of freedom, plus a fourth, which is translation in the direction of shear.

As indicated in Figure 15.12, each of the three vertical actuators is pinned at the bottom to a clevis which is bolted to the base plate. At the top, each is connected to its associated load cell through a spherical coupling. This arrangement is consistent with the three degrees of freedom identified above. Furthermore, for quick disassembly, the three actuator pins are removed, the two double flexures are detached, and the entire normal load frame with actuators attached can be



- 1. Vertical Load Cell No. 1
  - 2. Vertical Load Cell No. 2
  - 3. Vertical Load Cell No. 3
  - 4. Analog Summation of Total Vertical Normal Load
  - 5. Horizontal Load Cell
  - \*6. Horizontal Displacement of Top block Relative to Bottom Block - LVDT1
  - 8. Horizontal Displacement of Top Block Relative to Bottom Block - LVDT3
  - \*9. Vertical Relative Displacement Proximeter No. 4
  - \*10. Vertical Relative Displacement Proximeter No. 5
  - \*11. Vertical Relative Displacement Proximeter No. 6
  - \*12. Vertical Relative Displacement Proximeter No. 7
  - 13. Horizontal Acceleration at Near Left of Upper Specimen Block
- \* see Figure 2-4 for exact location

Figure 15.12. Loading apparatus for normal and direct shear testing of rock joints (basic mechanical apparatus)

hoisted up away from the specimen/roller box assembly. The apparatus is capable of applying mechanical normal loads of up to approximately 0.333 MN.

### **15.3.2.3 Horizontal Mechanical Load System**

The horizontal actuator produces direct shear to the upper specimen box via the horizontal load cell, which acts through a spherical coupling. This coupling allows for slight misalignment in the horizontal shearing motion. It also allows for elevation changes of the upper specimen due to vertical load, joint surface roughness, and progressive wear. Control of the horizontal actuator load for all tests described herein is based on the horizontal shear displacement.

### **15.3.2.4 Hydraulic System**

The hydraulic portion of the apparatus, which represents the modification to the basic direct shear apparatus, is designed to allow linear flow experiments to be conducted while the rock joint is undergoing normal or shear loading. As shown in Figure 15.13, the fluid is injected at a constant flowrate over the entire width of the fracture on the left edge of the top specimen, and collected over the entire width of the fracture from the right edge of the top specimen. The flowrate is chosen such that laminar flow is maintained within the fracture. For these MH experiments, a flowrate of 4.0 cc/min was determined to meet this criteria for all normal mechanical loadings. Absolute and differential pressure transducers are used to measure the inlet and outlet fluid pressures.

A rectangular rubber gasket is placed around the specimen to prevent water leakage. The reason for this gasket is that the lower block extends beyond the upper block, thus making it difficult to prevent water leakage especially during shearing of the upper block. Silicon grease and rubber cement are used to ensure that water does not leak out from above or below the rubber gasket. The apparatus is designed such that a finite normal load must be applied to compress the rubber gasket and allow the upper and lower rock joint surfaces to come into contact. This ensures adequate sealing of the system against leakage. The portion of the rubber gasket covering the joint along the front and back surfaces of the block is not shown in Figure 15.13 for clarity. In addition, the rubber along these two front and back surfaces is compressed with thin metal plates to prevent leakage of fluid from the joint along these surfaces.

Prior to grouting the specimens into the steel boxes, all five sides of the top and bottom rock blocks, except the joint surfaces themselves, are coated with a silicon rubber cement. The specimen (rock matrix and fracture) is then completely saturated with water prior to the MH experiment. This is done to maintain fluid flow for the most part only in the fracture, and prevent water leakage from the matrix.

### **15.3.2.5 Instrumentation and Control**

Instrumentation channels for the mechanical loading portion of the experiment are identified in Figure 15.12. The locations of various relative displacement sensors on the specimen are shown in Figures 15.14 and 15.15.

All load cells are typical commercial strain gage units with dominant sensitivity to tension/compression along one axis. Reaction to the applied static normal load is measured in terms of relative vertical displacements of the two blocks at four locations near the interface. Measurements near the interface are desirable to reduce the effect of the deformation of the intact rock,

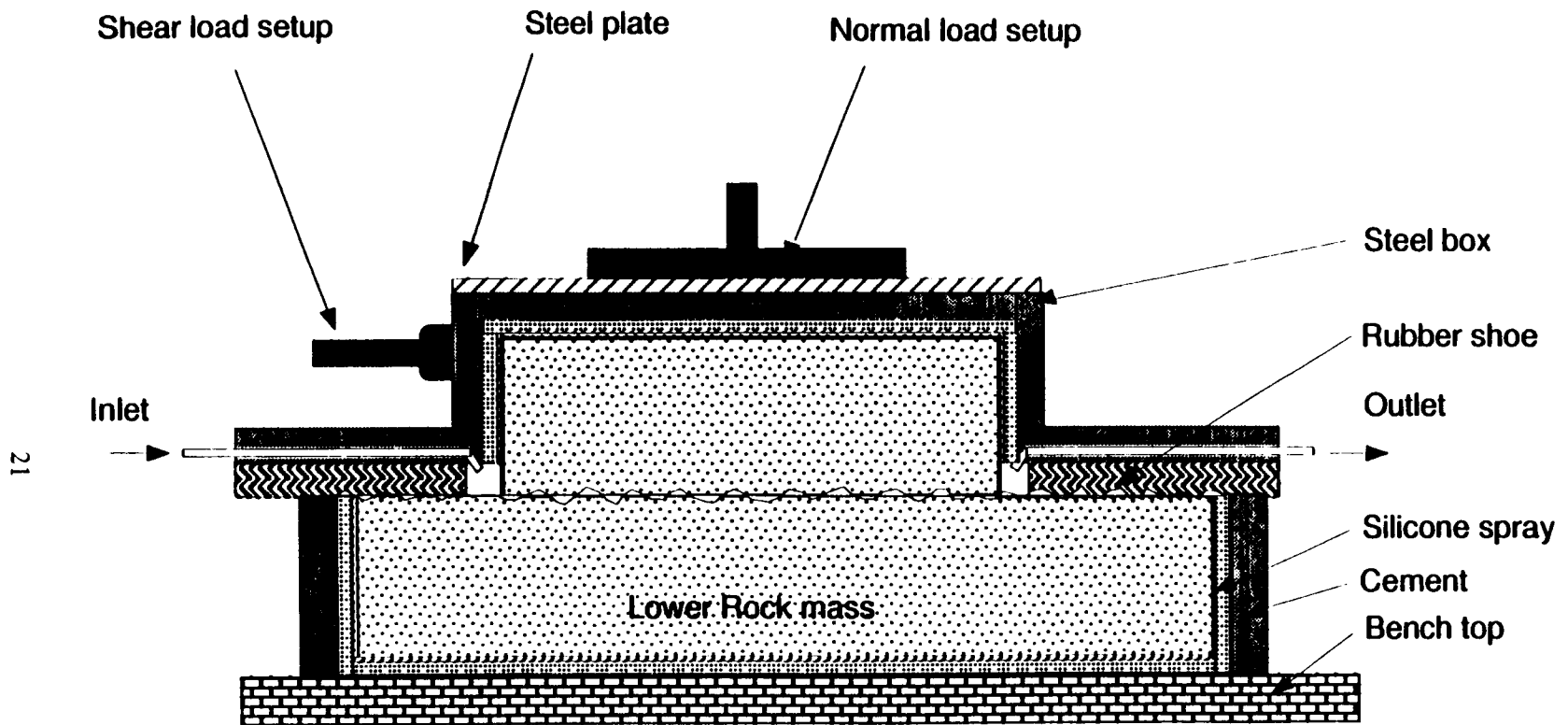


Figure 15.13. Schematic diagram of the linear flow apparatus with normal and shear loading arrangements.

such that only the joint deformation is measured. For this, the transducers are of proximity (non-contacting) eddy-current sensing type, since horizontal movement of the two surfaces must be allowed, but only vertical displacement changes must be sensed. Hence, the four vertical measurement points can be used to resolve the rigid body displacement of the upper block relative to the lower specimen block, according to the first three degrees of freedom identified earlier.

Vertical proximity transducers were mounted on each side near the joint interface as shown in Figures 15.14 and 15.15. As indicated in Figure 15.15, the specimen is grouted into the upper and lower boxes so that a 2.54 cm gap is left between the box faces. The interface, which varies from one specimen to another, is nominally enclosed within this gap. The sideplates of each half of the specimen box are slotted, so that vertical proximeter supports and target plates can be mounted directly onto the sides of respective halves of the specimen near the interface. Two prongs which support each plate component are cemented into lateral holes that are drilled into the specimen sides. Although some movement of the specimen within the grout occurs during loading, the side slots are large enough so that no interference occurs between the support prongs and the box side plates. Thus, as the upper box and associated target plates move horizontally relative to the lower specimen, change in vertical relative position is also sensed continuously. Furthermore, the heavy mounting frame for the upper box side rollers is slotted so that there is no interference between the frame and the target plates as the upper box displaces both horizontally due to shear and vertically due to unevenness and wear of the interface.

Relative shear displacements of the specimen blocks are measured by two LVDT's as indicated in Figure 15.16. LVDT1 is located at the near end of the specimen and measures displacement of the upper block relative to the lower block. Each half of the transducer is cemented directly into a hole drilled into the respective specimen block. LVDT2 is similarly mounted on the far side of the specimen pair, as shown in Figure 15.16. The output of these two transducers pro-

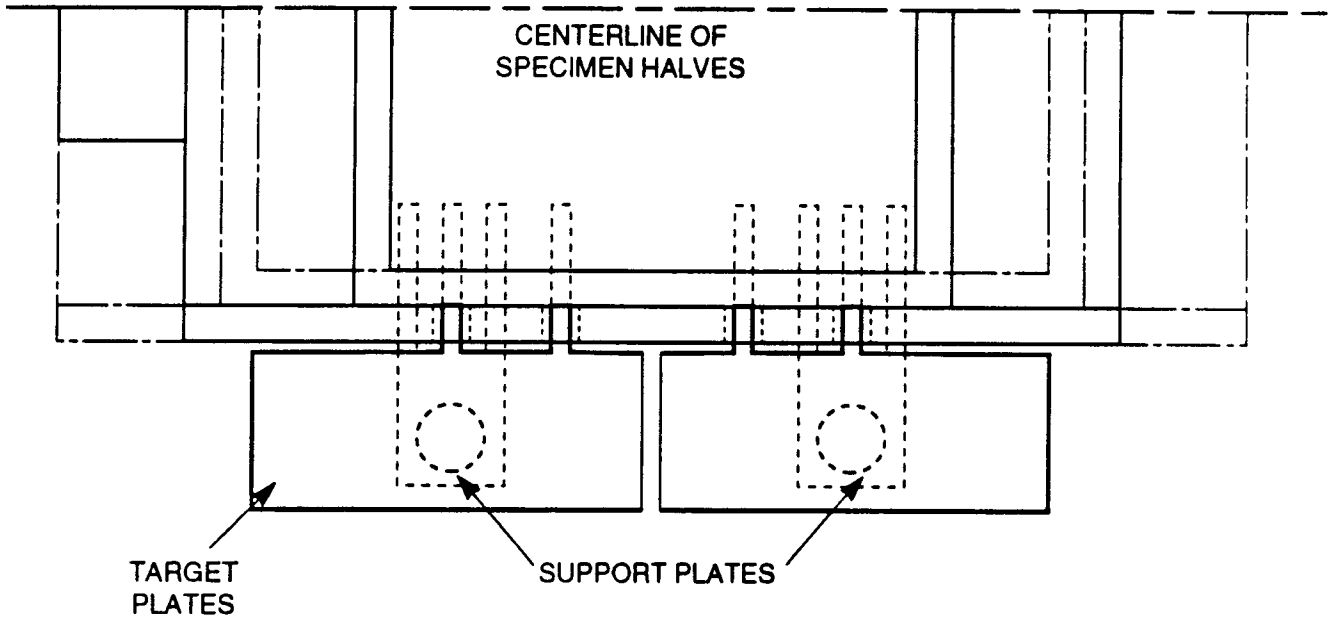


Figure 15.14. Top view of vertical displacement instrumentation supports and targets.

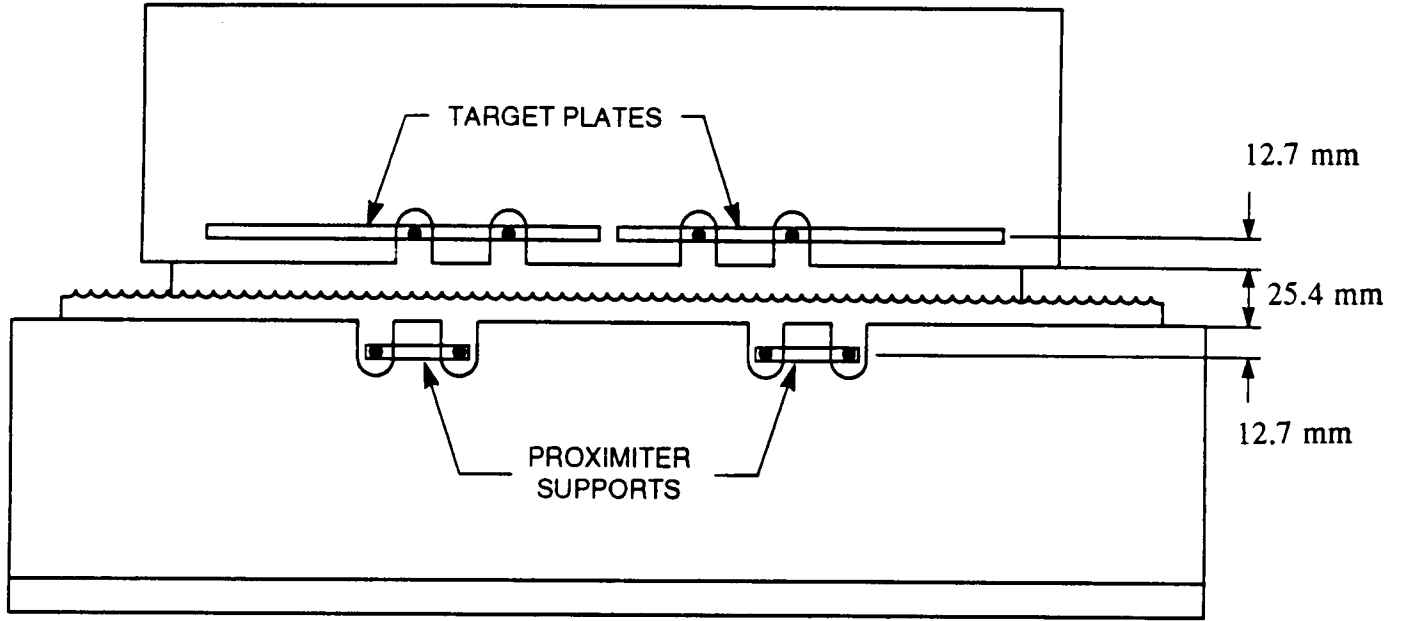


Figure 15.15. Side view of vertical displacement instrumentation supports and targets.

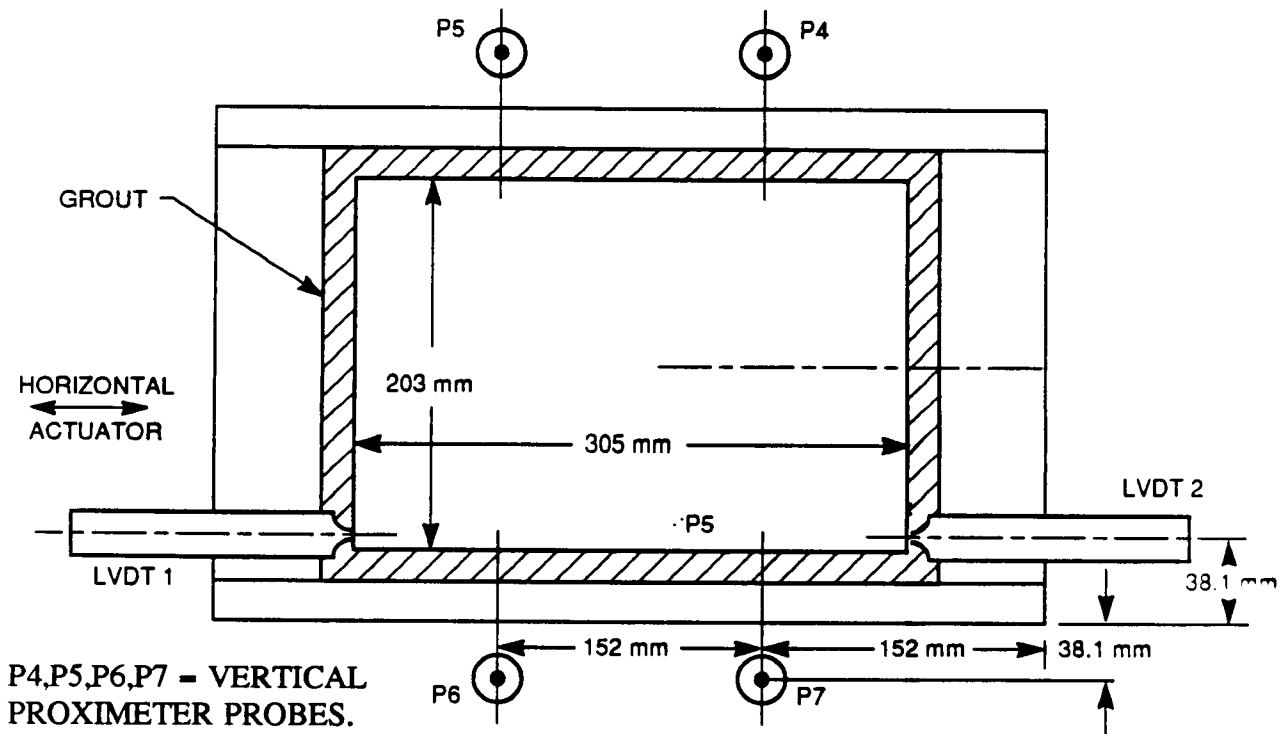


Figure 15.16. Location of relative displacement sensors on specimen lower block.

vides the direct shear movement of the joint interface. Control in all cases for the MH joint experiments was imposed on a prescribed horizontal displacement signal by applying a slow ramp to the relative displacement, while the force required was simultaneously recorded.

### 15.3.2.6 Mechanical Properties of Intact Rock

The rock specimens for the MH experiments were prepared from 45.7-cm-diameter core that was drilled from a road cut near Superior, Arizona (USA). The rock is a welded tuff of the Apache Leap formation. Statistical analysis on 113 uniaxial Apache Leap welded tuff samples and 72 triaxial specimens yielded the following average values for the mechanical rock properties, as shown below in Table 15.4.

**Table 15.4. Intact rock properties obtained from testing of welded tuff samples**

Young's Modulus E [GPa]	3.86±3.4
Poisson's Ratio [-]	0.20±0.029
Uniaxial Compressive Strength $C_o$ [MPa]	161.0±26.0
Triaxial Compressive Strength [MPa]	
- Confining Pressure 3.4 MPa	202.0±27.0
- Confining Pressure 6.9 MPa	248.0±22.0
- Confining Pressure 10.3 MPa	271.0±18.0
Uniaxial Tensile Strength $T_o$ [MPa]	10.3±2.2
Density [kg/m <sup>3</sup> ]	2420.0
Saturated Hydraulic Conductivity $k_s$ [m/s]	2.131±E-08
Effective Porosity	0.175

### 15.3.2.7 Mechanical Properties of the Rock Joint

The mechanical deformation of a typical rock joint is nonlinear in that the normal joint stiffness ( $K_n$ ) increases with increasing normal stress in a nonlinear fashion. The normal stiffness of the joint surface has been calculated from the experimental data obtained in normal deformation tests in the laboratory. Values of the normal stiffness have been calculated at the expected normal loads during each shear test based on the global slope of  $\sigma_n$  versus  $u_n$  curve (equivalent to the secant stiffness). These values are provided in Table 15.5 and are based on mean values from the fifth loading cycle for 19 jointed specimens tested. The shear stiffness,  $K_s$ , is the slope of the shear stress,  $\sigma_s$ , versus shear displacement,  $u_s$ , curve in the elastic (pre-peak) region. The shear stiffness is estimated from the experimental shear stress versus shear displacement curve obtained in the laboratory for each specimen with each normal stress applied on the specimen. The esti-

mated mean values from the 19 specimens tested at the expected normal loads to be conducted in the MH test are also given in Table 15.5. The estimated values are the global slope of the curve in the elastic region, that is, they are the secant stiffnesses of the joint at the given normal stress.

**Table 15.5. Estimated joint normal ( $K_n$ ) and shear stiffnesses ( $K_s$ ) at expected normal loads.**

Expected Normal Stress (MPa)	Normal Stiffness (GPa/m) (Secant)	Shear Stiffness (GPa/m) (Secant)
2.0	37.7±19.9	5.7±4.6
4.0	46.8±26.1	10.6±7.0
5.0	49.0±25.4	12.4±4.9

During shear deformation, the amount of joint dilation depends on many factors including the joint compressive strength, joint roughness, and applied normal load. For the mechanical experiments conducted on 19 naturally jointed, welded tuff samples, Table 15.6 provides the mean dilation angle as well as the maximum dilation and shear displacement corresponding to the maximum dilation at each of the expected normal loads for the MH experiment. Typically, the joints experience a small amount of closure at the onset of shear followed by joint dilation. The amount of initial closure increases with normal load. The dilation angle,  $\phi$ , has been calculated as the global slope (i.e., secant slope) of the dilation curve between zero dilation and maximum dilation.

**Table 15.6. Estimated values of dilation angle,  $\psi$ , with other parameters to describe the  $u_n$  versus  $u_s$  curves.**

Normal Stress (MPa)	Peak Dilation $u_{nmax}$ (mm)	Shear Disp. at Peak Dilation $u_{sdmax}$ (mm)	Dilation Angle, $\phi$ (degrees)
2.0	1.58±0.91	35.07±8.51	2.74±1.27
4.0	1.29±0.85	38.00±6.52	2.18±1.11
5.0	1.28±0.91	38.02±7.75	2.27±1.12

The cohesion,  $c$ , and friction angle,  $\phi$ , represent the strength of the rock joint. The mean values of the residual joint cohesion,  $c_r$ , and residual joint friction angle,  $\phi_r$ , were experimentally determined to be 0.10 MPa and  $39.6\pm 4.5^\circ$ , respectively.

Parameters for the BB joint model were also determined for both joint closure behavior and joint shear behavior. The joint closure under normal loads can be modeled empirically using hyperbolic loading and unloading curves relating the effective normal stress,  $\sigma_n$ , and joint closure,  $u_n$  as:

$$\sigma_n = \frac{u_n}{a - bu_n} \quad (15-8)$$

where  $a$  and  $b$  are empirical constants. The initial normal stiffness ( $K_{ni}$ ) and maximum allowable closure ( $u_m$ ) for each loading/unloading were determined through laboratory cyclic normal loading/unloading tests. Bandis et al. (1983) showed that  $K_{ni}$  of the joint is equal to the inverse of the constant  $a$  in Equation (5.8) and  $u_m$  is defined by  $a/b$ . The mean values of  $K_{ni}$  and  $u_m$  were determined from experimental tests of 19 welded tuff joints for the 5th normal load cycle to be  $24.7 \pm 12.7$  GPa/m and  $0.19 \pm 0.08$  mm, respectively. The joint shear behavior for the BB joint model is given by equation (15.2).

Barton and Choubey (1977) have proposed relations for JCS and  $\phi_r$  in this equation based on output from Schmidt-Hammer rebound tests. Using these relations, the mean values for JCS and  $\phi_r$  from 26 joint tuff samples were determined to be  $123.6 \pm 18.3$  MPa and  $26.6 \pm 1.2^\circ$ , respectively. The value of  $\phi_r$  using Barton and Choubey's relation is somewhat lower than previously derived applying the Coulomb relation. The initial  $JRC_o$  can be estimated using the following relation proposed by Barton and Choubey (1977):

$$JRC_o = \frac{\alpha - \phi_r}{\log\left(\frac{JCS}{\sigma_{no}}\right)} \quad (15-9)$$

where  $\alpha$  is the tilt angle, and  $\sigma_{no}$  is the corresponding effective stress calculated from the weight of the top block of the joint specimen when sliding occurs. The mean value for  $JRC_o$  from 12 specimens tested was calculated using Equation 5.9 to be  $5.93 \pm 1.18$ .

### 15.3.2.8 Characterization of Rock Joint Interfaces and Aperture

Surface profile measurements were taken of the joint surfaces on both the top and bottom specimens prior to conducting the MH test, as well as after completion of the direct shear tests. The scanning interval in both the x and y directions was set at 0.64 mm. The scanning window was the same for both the before and after profile measurements, such that direct comparisons could be made. Figures 15.17 and 15.18 show surface elevation plots of the top and bottom portion of the welded tuff specimen used for the MH test, respectively. Attempts were made to try to numerically mate the two upper and lower joint surfaces to facilitate calculation of the approximate initial aperture distribution over the joint area under zero applied normal stress. Based on this exercise, the mean aperture was determined to be approximately 0.032 in. (0.81 mm).

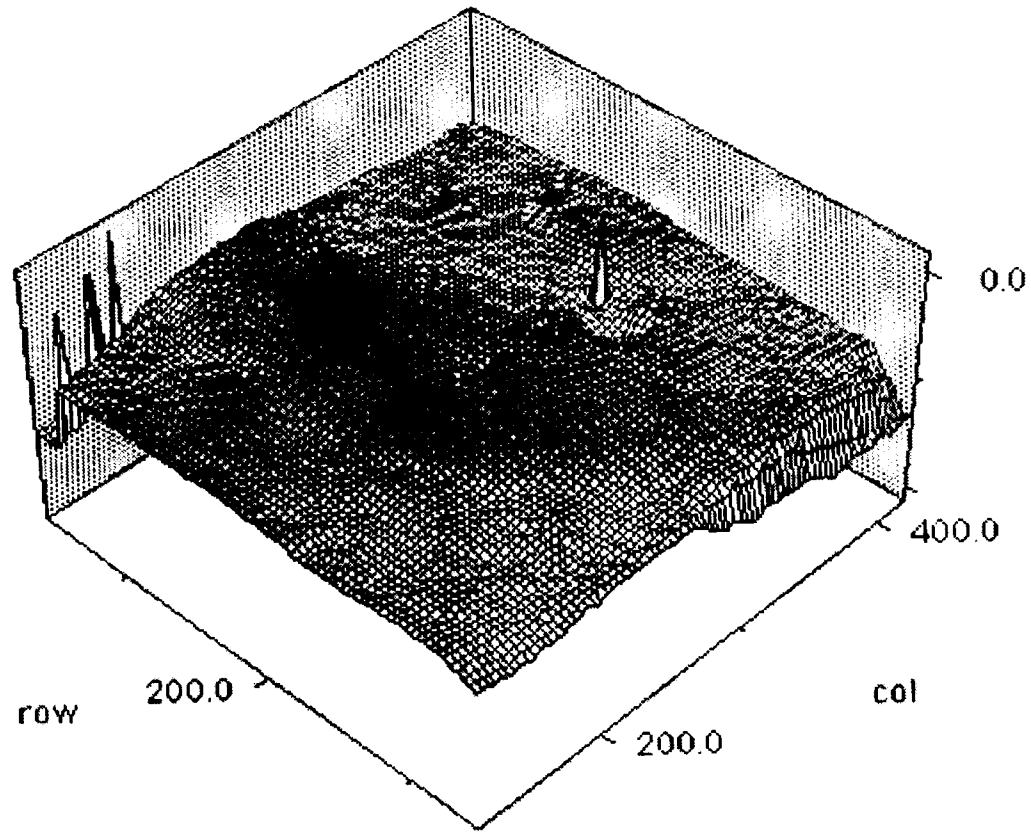


Figure 15.17. Surface profile data of the upper rock mass before initiation of the experiment.

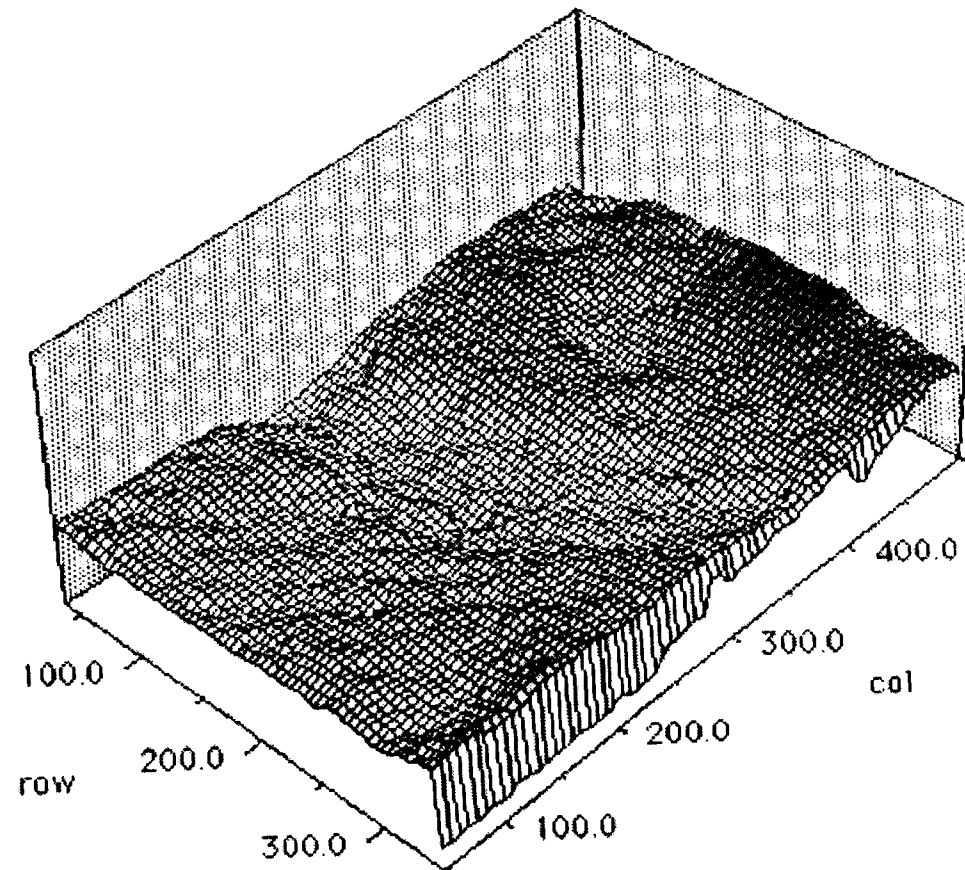


Figure 15.18. Surface profile data of the lower rock mass before the initiation of the experiment.

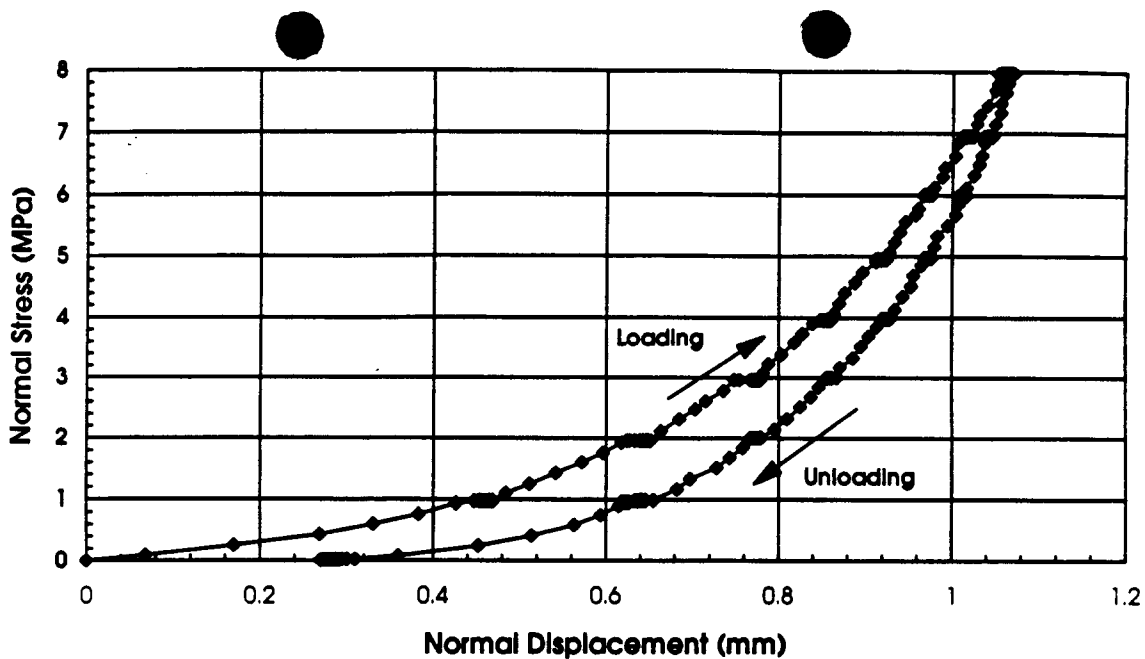


Figure 15.19. Mechanical response of joint under normal loading after many cycles of loading.

### 15.3.3 Experimental Results

#### 15.3.3.1 Joint Normal Loading

Joint normal loading was conducted up to a maximum load of 8.0 MPa while monitoring the joint normal displacement (i.e., joint closure) and fluid pressure changes across the sample for a fixed flowrate. Figure 15.19 shows the normal stress versus normal displacement response of the natural welded tuff rock joint, based on the average of the four vertical displacement proximeters. Prior to this particular normal load cycle, the joint had already undergone approximately five normal load cycles such that the joint could be considered to be well seated. Figure 15.19 shows that there is still some hysteresis between the loading and unloading portions, the unloading curve being below the loading curve. A maximum closure of approximately 1.08 mm is reached at the maximum normal stress of 8.0 MPa. The maximum closure appears to be somewhat higher than the mean value observed from pure mechanical normal load tests on similar welded tuff joints for the same cycle. The reason for this is unclear, however, it was noticed that readings from individual proximeters indicated that one end of the joint experienced much more normal closure than the other end. The component of normal stress necessary to compress the rubber gasket around the sample to prevent water leakage was subtracted out of the joint closure data and could possibly be the result of some error.

Figure 15.20 shows the corresponding normal stress versus effective hydraulic conductivity between the inlet and outlet edges of the joint. For the hydraulic portion of the test, the fluid flow rate was held fixed at 4.0 cm<sup>3</sup>/min. After each 1-MPa increment in normal stress, the normal stress was held fixed and the saturated flow test was conducted through the rock fracture. Flow measurements were made only after steady state conditions were reached. Thus, the hydrologic tests were conducted under pseudostatic conditions. A maximum pressure drop of approximately 300 Pa was measured at the maximum load (i.e., 8.0 MPa). There appears to be some hysteresis between the loading and unloading curves, although there is some scatter in the pressure measure-

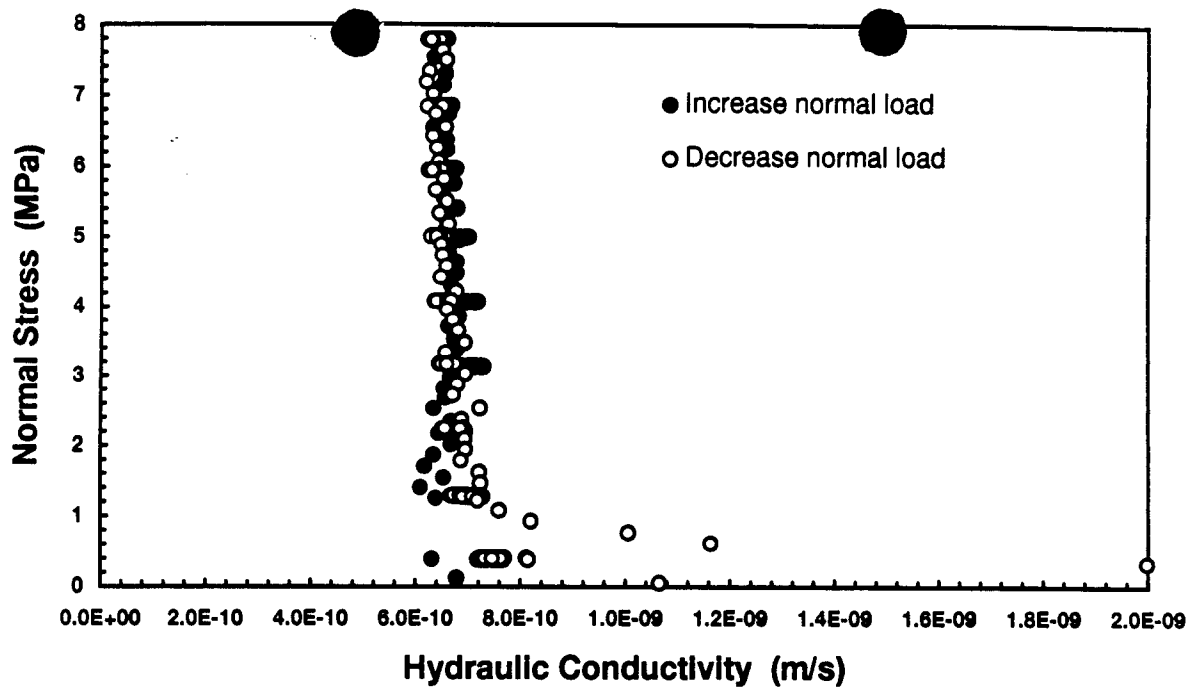


Figure 15.20. Hydraulic response of joint under normal loading after many cycles of loading.

ments. This is likely because the normal displacement as measured from the four vertical displacement proximeters is not uniform over the sample, indicating some degree of tilting of the top block during the normal loading/unloading procedure. This could easily cause fluctuations in the pressure drop measurements.

### 15.3.3.2 Joint Shear Loading

The shear deformation experiment initially encountered some problems with fluid leakage from the apparatus. The experiment was initially designed to conduct coupled shear-flow tests under normal stresses of 2.0, 4.0, and 5.0 MPa. However, it turned out that a total of four direct shear cycles under a constant normal stress of 2.0 MPa were performed before any confidence was reached regarding the results of the flow measurements. In other words, from the first three shear cycles in which the top block was sheared approximately 2.54 cm (1 in.) in the forward direction followed by shearing in the reverse direction back to the initial zero point, only mechanical data on the joint behavior was obtained. It should be pointed out that the top block is centered over the bottom block such that the bottom block extends 5.08 cm (2 in.) on either side in the direction of shear. Thus, during the shearing, the area of the sheared surface remains constant.

Figure 15.21 represents the first shear stress versus shear displacement cycle. For this particular specimen, a peak shear stress response does not occur. This is somewhat peculiar, since in almost all previous mechanical tests done on very similar jointed specimens of the same rock type, a peak shear stress response was observed during the first cycle. Thus, this particular test may not be representative. However, one possible reason for the absence of a peak shear stress is that fluid (water) exists along the fracture surface, which likely acts somewhat as a lubricant. It is also observed in Figure 15.21 that the residual shear stress upon reverse shearing is lower than that during forward shearing. Figure 15.22 shows the normal displacement (i.e., joint dilation) as a function of shear displacement for the four cycles conducted under a normal stress of 2.0 MPa. Some initial closure (i.e., negative displacement) occurs upon initiation of shearing, followed by opening of the joint. While the shear stress versus shear displacement curves are very similar among all four cycles under 2.0 MPa constant normal stress, the normal displacement versus

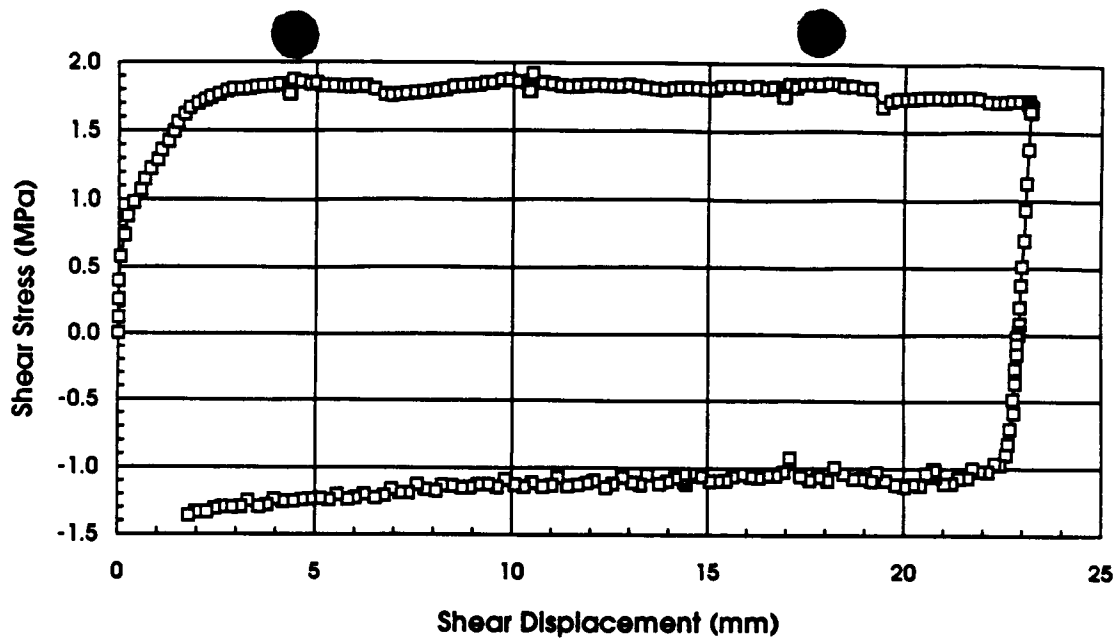


Figure 15.21. Mechanical response of rock joint for first shear loading cycle.

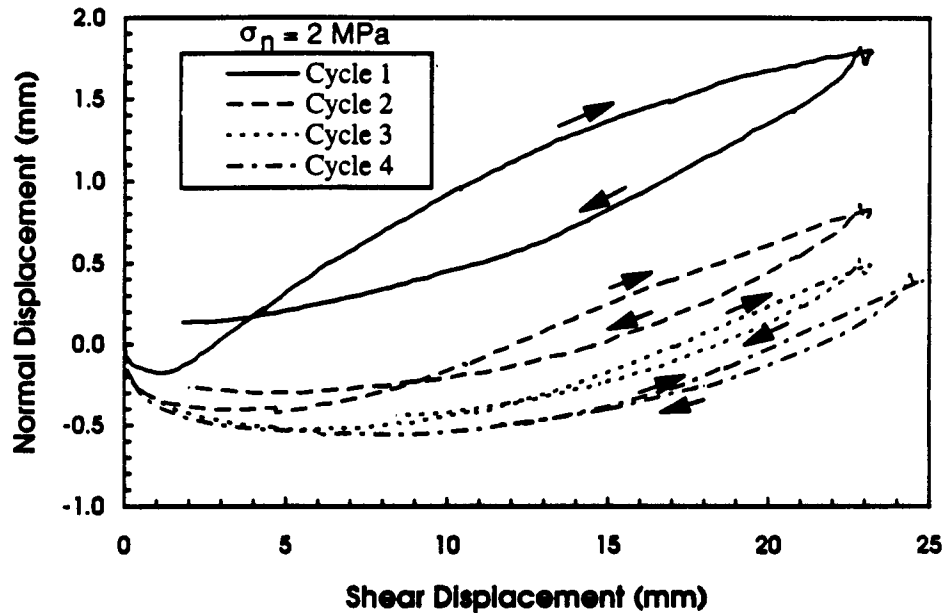


Figure 15.22. Dilation response of rock joint for first four shear cycles.

shear displacement curves are remarkably different. As the surface is worn down under repeated shear cycling, the amount of joint dilation also decreases, as shown in Figure 15.22. Presumably, at the same time, there is more and more gouge buildup within the joint. At the completion of four cycles of shearing, the apparatus was disassembled and it was verified that a significant amount of gouge material had collected within the joint. The maximum joint dilation is measured to be 1.8, 0.8, 0.45, and 0.35 mm for the first four shear cycles, respectively. Again, this maximum dilation represents an average of the four vertical displacement proximeters.

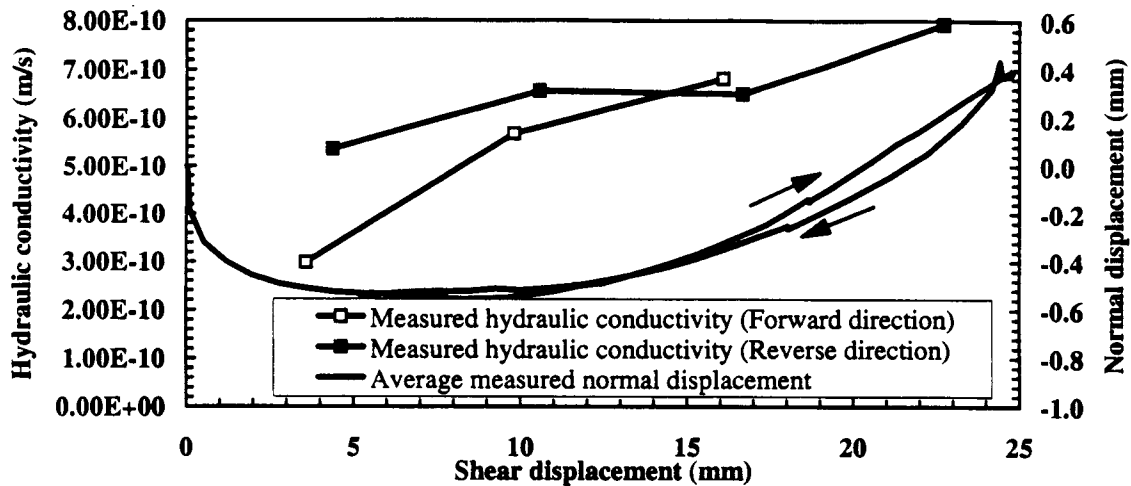


Figure 15.23. Hydraulic response and mechanical dilation of rock joint during fourth shear cycle under constant applied normal stress of 2.0 MPa.

It was only for the fourth cycle that corresponding hydraulic data was obtained. Figure 15.23 shows the change in joint hydraulic conductivity with shear displacement in both the forward and reverse directions for this fourth cycle. The dilation curve has also been superimposed on the figure to aid in the interpretation. To obtain the hydrologic data, steady state pressure measurements across the length of the fracture were taken after each 6.35-mm (0.25-in.) increment in shear displacement. During the forward shear movement of 25 mm, the available data show an increase in hydraulic conductivity of approximately 51 percent. Again, one would expect a much larger increase in hydraulic conductivity if data was available for the first shear cycle, in which the maximum dilation was over five times greater than that for the fourth cycle. During reverse shearing, the hydraulic conductivity drops by a factor of approximately 2.5 from the value measured at the maximum shear displacement of 25 mm. This fairly large change in hydraulic conductivity most likely is attributed to wearing down of asperities thus decreasing the effective hydraulic aperture and the gouge material buildup within the joint. However, the experiment was not able to discriminate between which had the greater effect.

Additional shearing was conducted under normal stresses of 4.0 and 5.0 MPa. Figure 15.24 shows the shear stress versus shear displacement response under these two applied normal stresses (cycles 5 and 6) in addition to that just described for the fourth shear cycle. During these latter shear cycles, the reverse shear displacement was limited to only 19 mm (0.75 in.). This was done because large rises in pressure were experienced at the end of the shear cycles (back near the initial starting point), which began to exceed the range of the pressure gauges. This was found to be due to the accumulation of gouge material within the joint. Also, at the higher normal stresses, even though the maximum displacement of 25 mm was measured from the horizontal actuator, the measured relative shear displacement along the joint fell short of this value at the higher normal stress loadings of 4.0 and 5.0 MPa as shown in Figure 15.24. The reason for this is that there is some amount of compliance in the apparatus, especially in the steel boxes and grout surrounding welded tuff specimens. The 4th shear cycle is very smooth since repeated cycling was done at this normal stress loading of 2.0 MPa and one would not expect much additional asperity break-

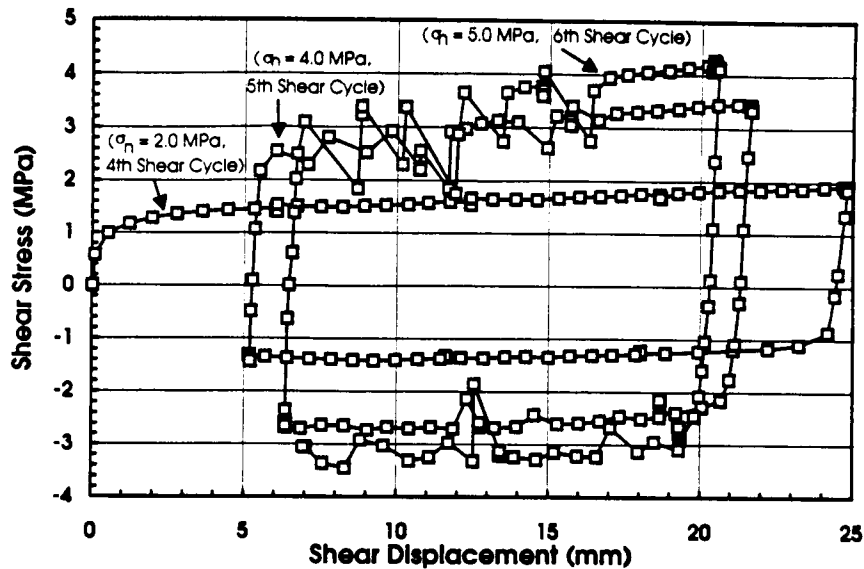


Figure 15.24. Mechanical response for shear loading under different applied normal stresses.

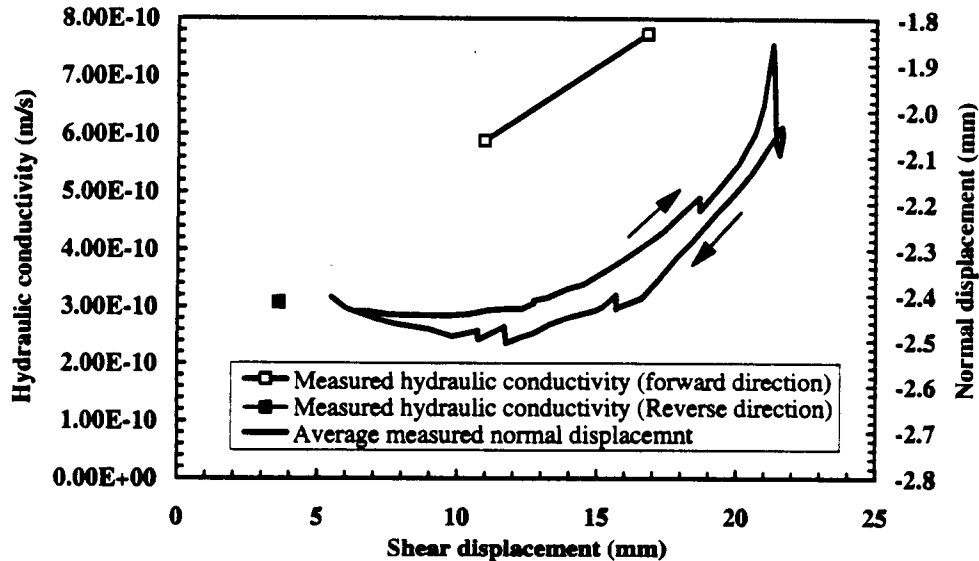


Figure 15.25. Hydraulic response and mechanical dilation of rock joint for the fifth shear loading cycle under 4.0 MPa normal stress.

age. However, the 5th and 6th shear cycles under higher normal loadings show fluctuations in the shear load due to stick-slip behavior as well as shearing (breakage) of asperities causing a temporary reduction in shear load.

Figures 15.25 and 15.26 show both the normal displacement and hydraulic conductivity plotted against shear displacement for shear cycles 5 and 6, which correspond to normal applied stresses of 4.0 and 5.0 MPa. In these plots, the normal displacement is the average reading from the four vertical displacement proximeters. Again, each of these two shear cycles began at

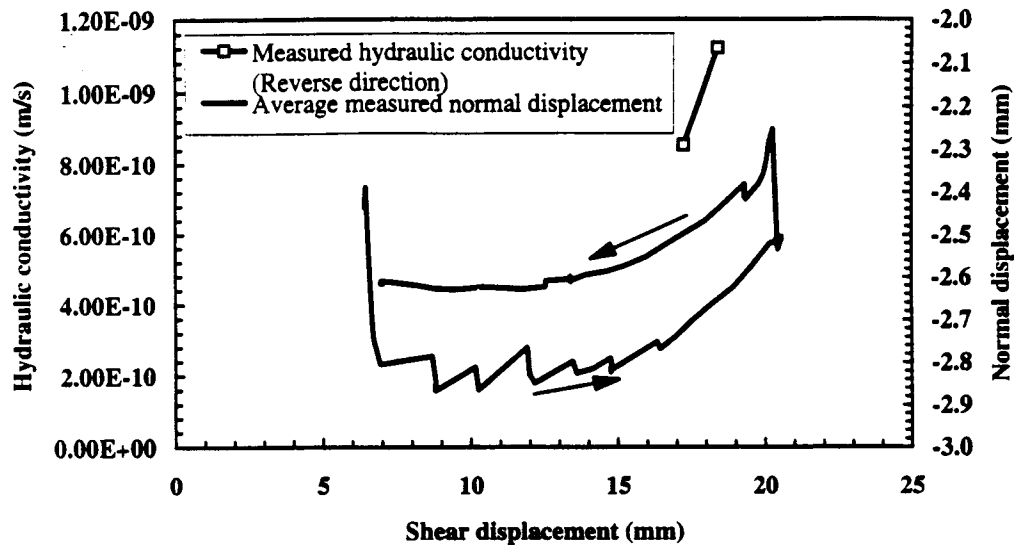


Figure 15.26. Hydraulic response and mechanical dilation of rock joint for the fifth shear loading cycle under 5.0 MPa normal stress.

approximately 6.35 mm to the right of the initial mated position for reasons explained earlier. At these higher normal loads, more problems were encountered with water leakage such that fluid pressure drop measurements could be made at only a few discrete shear displacement locations as indicated in Figures 15.25 and 15.26. From the available data, there appears to be consistency with hydraulic conductivity measurements obtained under the normal stress of 2.0 MPa (i.e., Figure 15.23), namely that during the reverse shearing there is a noticeable decrease in the fracture hydraulic conductivity.

#### 15.3.4 Numerical Simulation Results for TC5

Numerical simulation of the mechanical response portion TC5 was conducted using the 3D finite element code ABAQUS (Hibbitt, Karlsson & Sorensen, 1992). The code has the capability to explicitly represent joints using interface or gap elements, however, such elements model strictly Mohr-Coulomb type behavior, and do not allow dilation along the joint. As a result, for the analysis of this TC problem, it was decided to model the joint as a thin zone of continuum solid elements assigned various constitutive models available within ABAQUS. The width of this zone was arbitrarily set equal to 13 mm. The first analysis was conducted by applying the jointed material model within ABAQUS to this thin zone. This particular model is intended to provide a simple, continuum representation of material containing a high density of parallel joint surfaces in different orientations. In the case of this TC5 problem, a single orientation was taken along the horizontal plane of the actual rock joint tested. The spacing of the joints of a particular orientation is assumed to be sufficiently close compared to characteristic dimensions in the zone of the model that the joints can be integrated into a continuum of slip systems. The model provides for opening of the joints as well as frictional sliding. In the case of frictional sliding, the failure surface ( $f$ ) of a particular joint system is defined by

$$f = \tau - p \tan \beta - d = 0 \quad (15-10)$$

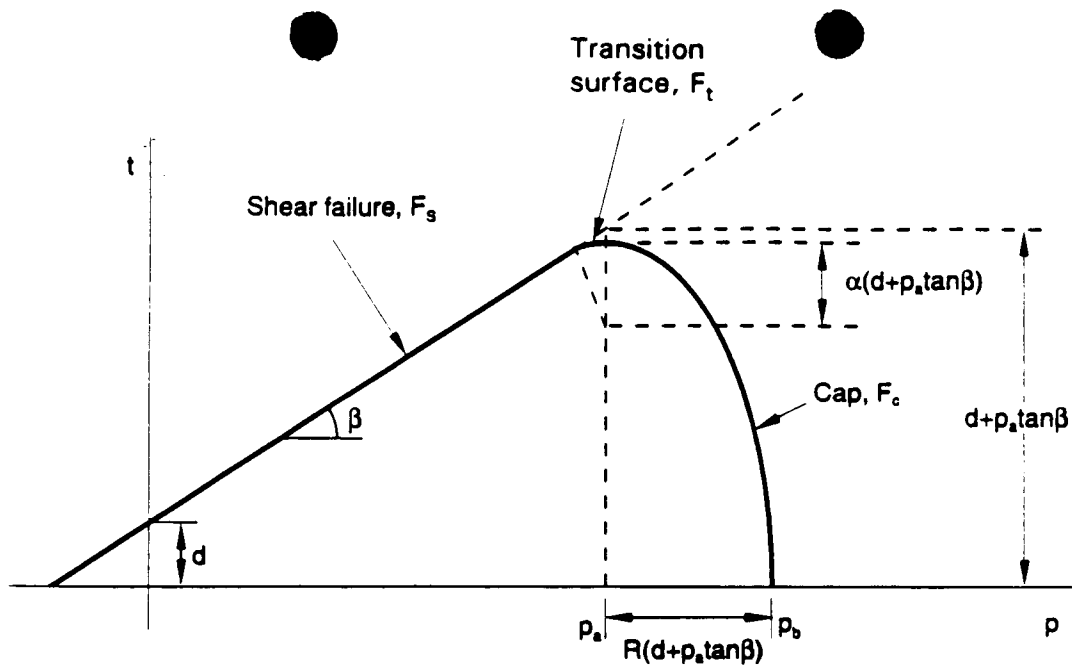


Figure 15.27. Modified Drucker-Prager/Cap model: yield surfaces in the  $p$ - $t$  plane.

where  $\tau$  is the magnitude of the shear stress resolved onto the joint surface,  $p$  is the normal pressure acting across the joint,  $\beta$  is the friction angle for the joint system, and  $d$  is the cohesion for the system. When  $f = 0$ , the joint system slips, and inelastic plastic strain develops. Dilation of the joint system during shearing will result if a positive dilation angle is specified. In addition to the joint systems, the model includes a bulk material failure mechanism, which is based on the Drucker-Prager failure criterion. The primary input parameters for this particular model are thus the friction angle, the cohesion, and the dilation angle of the joint system.

A second ABAQUS analysis was run using the modified Drucker-Prager/Cap plasticity model in ABAQUS in place of the jointed material model. The cap surface serves to: (i) bound the yield surface in hydrostatic compression, thus providing an inelastic hardening mechanism to represent plastic compaction, and (ii) control volume dilatancy when the material yields in shear, by providing softening as a function of the inelastic volume increase created as the material yields on the Drucker-Prager shear failure surface. The yield surface thus has two principal segments: a pressure dependent Drucker-Prager shear failure segment, and a compression cap segment, as shown in Figure 15.27. The Drucker-Prager failure segment itself is a perfectly plastic yield surface (no hardening) but plastic flow on this segment produces inelastic volume increase that causes the cap to soften. The Drucker-Prager shear failure surface ( $F_s$ ) is written as

$$F_s = t - p \tan \beta - d = 0 \quad (15-11)$$

where  $\beta$  and  $d$  represent the angle of friction of the material and its cohesion. The deviatoric stress measure  $t$  is defined as

$$t = \frac{1}{2}q \left[ 1 + \frac{1}{K} - \left( 1 - \frac{1}{K} \right) \left( \frac{r}{q} \right)^3 \right] \quad (15-12)$$

where

$p = \frac{1}{3} \text{trace } \underline{\sigma}$  is the equivalent pressure stress,

$q = \sqrt{\frac{3}{2}} S \cdot S$  is the Mises equivalent stress,

$r^3 = \frac{9}{2} S : S \cdot S$  is the third stress invariant, and

$S = pI + \underline{\sigma}$  is the deviatoric stress.

$\underline{\sigma}$  = 3D stress tensor.

The material parameter  $K$  is the ratio of the yield stress in triaxial tension to the yield stress in triaxial compression, and controls the dependence of the yield surface on the value of the intermediate principal stress. The value of  $K$  must lie in the range 0.778 to 1.0 (Hibbitt, Karlsson & Sorenson, 1992).

The cap yield surface has an elliptical shape and hardens or softens as a function of the volumetric plastic strain: volumetric plastic compaction (when yielding on the cap) causes hardening, while volumetric plastic dilation (when yielding on the shear failure surface) causes softening. The cap yield surface ( $F_c$ ) is written as

$$F_c = \sqrt{[p - p_a]^2 + \left[ \frac{Rt}{(1 + \alpha - \alpha / (\cos \beta))} \right]^2} - R(d + p_a \tan \beta) = 0 \quad (15-13)$$

The material parameters  $R$  and  $\alpha$  are small numbers which control the shape of the cap and the transition between the cap and shear yield surfaces, respectively. For this particular plasticity model, the user must define a piecewise linear function for the hardening/softening law relating the hydrostatic compression yield stress and volumetric plastic strain. This hardening/softening law can be related to the pressure term  $p_a$  in the above equation as discussed by Hibbitt, Karlsson & Sorensen (1992). In the modeling of TC5, the parameters  $K$ ,  $R$ , and  $\alpha$  were not well known, however, the applicable range of values for these parameters was small. As such, sensitivity analyses showed that their particular values had little effect on the outcome of the TC5 analysis. The outcome of the analysis was primarily governed by the values specified for the friction angle  $\beta$ , the cohesion  $d$ , and the user defined hardening/softening law. Unlike the jointed material model, the Drucker-Prager/Cap plasticity model implemented in ABAQUS does not require a dilation angle as input. The amount of dilation is governed by user defined cap hardening/softening law

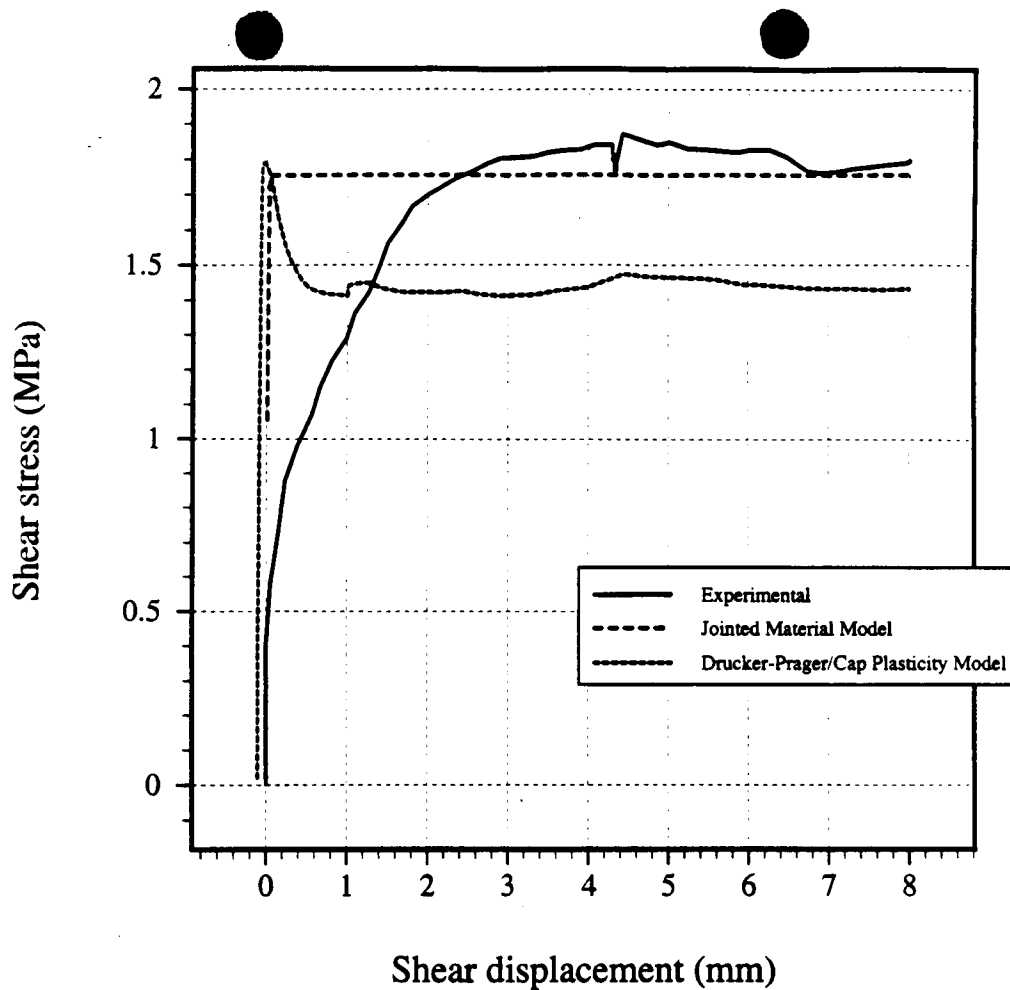


Figure 15.28. Comparison between experimental and numerical results for the shear strength of joint during first cycle.

In using the jointed material constitutive model, the Mohr-Coulomb parameters, namely the friction angle  $\phi$  and cohesion  $c$  obtained from the mechanical properties testing of the joints (see Section 15.2.2.8), are used for the friction angle  $\beta$  and cohesion  $d$  in Equation 15.11. However, for the Drucker-Prager/Cap plasticity model, the friction angle  $\phi$  and cohesion  $c$  for the Mohr-Coulomb model must be converted into equivalent values for the Drucker-Prager model (Equation 15.12). In doing so, the approach was taken to match the two models to provide the same failure behavior in triaxial compression and tension (Hibbitt, Karlsson & Sorenson, 1992). Matching the two models to provide the same flow and failure response in plane strain resulted in the Drucker-Prager model significantly underestimating the shear strength of the joint. This is because the experiment itself is not truly two dimensional.

Figure 15.28 shows a comparison of the shear stress versus shear displacement response between the experimental measurements and those predicted by ABAQUS for the first shear cycle under the constant applied normal stress loading of 2.0 MPa. A shear displacement of only 8.0 mm was carried out in the numerical simulation versus 25 mm in the actual experiment. This is because the joint is represented as a thin shear zone using continuum elements, which restricts

the amount of shear deformation to avoid overly distorting the elements making up the joint. This is the primary limitation in using this type of approach to representing the joint behavior. The numerical results obtained using the modified Drucker-Prager/Cap model shows a distinct peak shear response followed by a reduction in shear stress, which eventually levels off at a residual value. This reduction in shear stress is due to softening along the cap yield surface as the joint dilates under shear. The experimental results show that the residual shear stress is substantially higher than that predicted by the Drucker-Prager/Cap model. However, the maximum shear stress predicted by ABAQUS corresponds closely with that of the experimental results, although it is reached after a much smaller shear displacement than the experimentally measured maximum. For this analysis, the elastic properties of the joint material were specified the same as that of the intact rock. Reducing the stiffness for the joint material would shift the peak shear stress response closer to the experimental value. Figure 15.28 also shows the ABAQUS numerical results based on representing the joint using the jointed material model. This model provides a close match with the residual stress obtained from the experimental measurements, provided that the Coulomb friction angle and cohesion properties are specified for the jointed material model. Again, the peak shear is reached right at the onset of shearing which could be delayed somewhat by reducing the joint stiffness. Unlike the Drucker-Prager model, no softening of the joint under shear is present.

Regarding dilation, the experimental results (as depicted in Figure 15.22) show the joint initially closing under shear, which cannot be simulated by either of the two constitutive models. It was found from initial numerical results that the maximum amount of dilation obtained by the Drucker-Prager/Cap model is significantly lower than that measured experimentally for this first shear cycle. Again, the dilation in this model is controlled by the user defined cap hardening/softening law. This piecewise curve is obtained from the experimental data for the loading portion of the normal stress versus normal displacement curve (Figure 15.19). Thus, the Drucker-Prager/Cap model is calibrated to the normal load/normal deformation curve, and the subsequent shear response is predicted. However, initial results indicate that if calibration to the normal joint deformation is done, the model still significantly underestimates the dilation under shear deformation. For the jointed material model, a dilation angle is required as input to the analysis. From the joint material properties given in Table 15.6, a joint dilation angle (secant) based on an applied normal stress across the joint of 2.0 MPa would be approximately equal to  $2.7^\circ$ . However, using this low dilation angle for this jointed material model in ABAQUS results in the solution being non-convergent because the stiffness matrix becomes less symmetric if the difference between the material friction angle and dilation angle is large. For associated plastic flow, where the dilation angle and material friction angles are equal, the model converges well. Using a higher dilation angle would result in the numerical results greatly over predicting the actual measured dilation along the joint.

## 15.4 CONCLUSIONS

The results of two separate experimental studies on the MH behavior of natural rock joints under shear deformation have been presented. The joints tested had varying degrees of surface roughness as well as different material properties. In addition, to the extent possible, attempts were made to compare various computer codes with different joint constitutive models against the experimental results to assess whether these constitutive models correctly model the actual joint behavior.

For TC1, despite the fact that the NGI CSFT test is a well defined laboratory experiment, several assumptions with respect to the material properties and specifically the boundary condi-

tions had to be made by the modeling teams. Both modeled joints show some deviation from the BB joint model. The deviation might be caused by the joint itself, or the way the joint behaves in the CSFT apparatus. A computer program will be able to reproduce the measured joint behavior if the assigned constitutive joint behavior model is appropriate. With regard to shear deformation, both TC1:1 and TC1:2 results show that dilation and changes in hydraulic aperture are not well modeled. However, NGI is close to the upper bound of the experimentally measured hydraulic apertures in TC1:1, whereas LBL is in close agreement with experimentally measured residual hydraulic apertures in TC1:2. All teams had to overcome difficulties related to the application of the boundary conditions. The strong influence of the various approaches on the final results has been demonstrated.

The TC5 experimental results show that the hydraulic properties of the joint can change by up to a factor of 3 under shear deformation. However, additional tests and improvements to the experimental apparatus are necessary in order to make more quantitative assessments of changes in such properties during shear and production of gouge. The numerical results obtained using ABAQUS show that, although the joints can be represented by thin zones having plastic or jointed material behavior, there appear to be several limitations in both the type of shear stress-shear displacement and dilation behavior obtained. Future work should look into enhancing explicit modeling of joints within ABAQUS to better handle the joint behavior under shear.

## 15.5 REFERENCES

- Bandis, S., A.C. Lumsden, and N. Barton. 1983. Fundamentals of Rock Joint Deformation. *Int. J. Rock Mech. Min. Sci. & Geomech. Abstr.* Vol. 20. pp. 244-268.
- Barton, N., S. Bandis, and K. Bakhtar. 1985. Strength Deformation and Conductivity Coupling of Rock Joints. *Int. J. Rock Mech. Min. Sci. & Geomech. Abstr.* Vol. 22. pp. 121-140.
- Barton, N.R. and V. Choubey. 1977. The shear strength of rock joints in theory and practice. *Rock Mechanics.* Vol. 10. pp. 1-54.
- Boulon, M.J., A.P.S. Selvadurai, H. Benjelloun, and B. Feuga. 1993. Influence of Rock Joint Degradation on Hydraulic Conductivity. *Int. J. Rock Mech. Min. Sci. & Geomech. Abstr.* Vol. 30. No. 7. pp 1311-1317.
- Buscheck, T.A., and J.J. Nitao. 1993. The analysis of repository-heat-driven hydrothermal flow at Yucca Mountain. *Proceedings of the 4th High-Level Radioactive Waste Management Conference.* New York, NY: American Society of Civil Engineers.
- Cook, N.G.W. 1992. *Natural Joints in Rock: Mechanical, Hydraulic, and Seismic Behavior and Properties under Normal Stress.* *Int. J. Rock Mech. Min. Sci. & Geomech. Abstr.* Vol. 29. No. 3. pp. 198-223.
- Cundall, P., and R.D. Hart. 1985. *Development of Generalized 2-D and 3-D Distinct Element Programs for Modeling Jointed Rock.* Itasca Consulting Group. Misc. paper SL-85-1. Vicksburg, MS: U.S. Army Corps of Engineers.
- Esaki, T., H. Hojo, T. Kimura, and N. Kameda. 1991. *Shear-flow coupling test on rock joints.* Seventh International Congress on Rock Mechanics. Aachen, Germany. Vol. 1. Ed. W. Wittke. pp. 389-392. Rotterdam, Netherlands: A.A. Balkema.
- Esaki, T., K. Ikusada, and A. Aikawa. 1992. *Surface roughness and hydraulic properties of sheared rock.* Fractured and Jointed Rock Masses. Lake Tahoe, California. Vol. 2. pp. 366-372.

- Goodman, R.E. 1976. *Methods of Geological Engineering in Discontinuous Rock*. St. Paul, MN: West Publishing Company.
- Guvanasen, V., and T. Chan. 1990. Three-dimensional Finite Element Solution for Heat and Fluid Transport in Deformable Rock Masses with Discrete Fractures. *Proc. Int. Conf. Computer Methods and Advances in Geomechanics*. pp. 1547-1552.
- Hibbitt, Karlsson & Sorenson, Inc. 1992. ABAQUS/Standard User's Manual. Version 5.3. Pawtucket, RI: Hibbitt, Karlsson, & Sorenson, Inc.
- Hoek, E., and J.W. Bray. 1981. *Rock Slope Engineering*. Third Edition. The Institute of Mining and Metallurgy, London, UK:358.
- Hsiung, S.M., W. Blake, A.H. Chowdhury, and T.J. Williams. 1992a. *Effects of Mining-Induced Seismic Events on a Deep Underground Mine*. Pure and Applied Geophysics. Vol. 139. pp. 741-762.
- Hsiung, S.M., A.H. Chowdhury, W. Blake, M.P. Ahola, and A. Ghosh. 1992b. *Field Site Investigation: Effect of Mine Seismicity on a Jointed Rock Mass*. CNWRA 92-012. San Antonio, TX: Center for Nuclear Waste Regulatory Analyses.
- Hsiung, S.M., D.D. Kana, M.P. Ahola, A.H. Chowdhury, and A. Ghosh. 1993. *Laboratory Characterization of Rock Joints*. CNWRA 93-013. San Antonio, TX: Center for Nuclear Waste Regulatory Analyses.
- Jing, L., J. Rutqvist, O. Stephansson, C.F. Tsang, and F. Kautsky. 1993. *DECOVALEX - Mathematical Models of Coupled T-H-M Processes for Nuclear Waste Repositories - Report of Phase I*. SKI Technical Report 93:31. Stockholm, Sweden: Swedish Nuclear Power Inspectorate (SKI).
- Jing, L., J. Rutqvist, O. Stephansson, C.F. Tsang, and F. Kautsky. 1994. *DECOVALEX - Mathematical Models of Coupled T-H-M Processes for Nuclear Waste Repositories - Report of Phase II*. (in publication). Stockholm, Sweden: Swedish Nuclear Power Inspectorate (SKI).
- Kana, D.D., D.C. Scheidt, B.H.G. Brady, A.H. Chowdhury, S.M. Hsiung, and B.W. Vanzant. 1990. *Development of a Rock Joint Shear Test Apparatus*. CNWRA 90-005. San Antonio, TX: Center for Nuclear Waste Regulatory Analyses.
- Kana, D.D., B.H.G. Brady, B.W. Vanzant, and P.K. Nair. 1991. *Critical Assessment of Seismic and Geomechanics Literature Related to a High-Level Nuclear Waste Underground Repository*. NUREG/CR-5440. Washington, DC: Nuclear Regulatory Commission.
- Landanyi, B., and G. Archambault. 1970. Simulation of shear behavior of a jointed rock mass. *Proc. 11th Symp. Rock Mech.* p. 105. Rotterdam: Netherlands, A.A. Balkema.
- Makurat, A. 1985. The effect of shear displacement on permeability of natural rough joints. Hydrogeology of rocks of low permeability. *Proc. 17th Int. Congr. Hydrogeol.*, Tucson, Ariz. pp. 99-106.
- Makurat, A., N. Barton, N.S. Rad, and S. Bandis. 1990. Joint conductivity variation due to normal and shear deformation. *Proceedings of the International Symposium on Rock Joints*. Leon, Norway. pp. 535-540. N. Barton and O. Stephansson (eds). Netherlands, Rotterdam: A.A. Balkema.
- Makurat, A., N. Barton, G. Vik, P. Chryssanthakis, and K. Monsen. 1990b. Jointed rock mass modeling. *Proceedings of the International Conference on Rock Joints*. N. Barton and O. Stephansson, eds. Leon, Norway. pp. 647-656.

- Makurat, A., M. Ahola, K. Khair, J. Noorishad, L. Rosengren, and J. Rutqvist. 1995. The DECOVALEX Test-Case One. *Int. J. Rock Mech. Min. Sci. & Geomech. Abstr.* (in publication).
- Mohanty, S., A.H. Chowdhury, S.M. Hsiung, and M.P. Ahola. 1994. *Single Fracture Flow Behavior of Apache Leap Tuff Under Normal and Shear Loads*. CNWRA 94-024. San Antonio, TX: Center for Nuclear Waste Regulatory Analyses.
- Noorishad, J., C.F. Tsang, and P.A. Witherspoon. 1984. A coupled thermal-hydraulic-mechanical finite element model for saturated fractured rocks. *J. Geoph. Res.* Vol. 89. No. B12. pp. 10365-10373.
- Rasmussen, T.C., D.D. Evans, P.J. Sheets, and J.H. Blanford. 1990. *Unsaturated Fractured Rock Characterization Methods and Data Sets at the Apache Leap Tuff Site*. NUREG/CR-5596. Washington, DC: U.S. Nuclear Regulatory Commission.
- Tsang, Y.W. and P.A. Witherspoon. 1981. Hydromechanical behavior of a deformable rock fracture subject to normal stress. *Journal of Geophysical Research*. Vol. 86. No. B10. pp. 9287-9298. American Geophysical Union.
- Teufel, W. T. 1987. Permeability changes during shear deformation of fractured rock. *28th US Symposium on Rock Mechanics*. pp. 473-480. Rotterdam, Netherlands: A.A. Balkema.